Contents lists available at ScienceDirect

Colloids and Surfaces B: Biointerfaces

Charge-switchable cell-penetrating peptides for rerouting nanoparticles to glioblastoma treatment

Maria Mendes [a,b], Sandra Nunes [b], Tânia Cova [b], Francisco Branco [a], Michael Dyrks [c], Beate Koksch [c], Nuno Vale [d,e,f], João Sousa [a,b], Alberto Pais [b], Carla Vitorino [a,b,*]

[a] Faculty of Pharmacy, University of Coimbra, Pólo das Ciências da Saúde, Azinhaga de Santa Comba, Coimbra 3000-548, Portugal
[b] Coimbra Chemistry Centre, Institute of Molecular Sciences - IMS, Faculty of Sciences and Technology, University of Coimbra, Coimbra 3004-535, Portugal
[c] Freie Universität Berlin, Institute of Chemistry and Biochemistry, Arnimallee 20, Berlin 14195, Germany
[d] PerMed Research Group, Center for Health Technology and Services Research (CINTESIS), Rua Doutor Plácido da Costa, 4200-450 Porto, Portugal
[e] CINTESIS@RISE, Faculty of Medicine, University of Porto (FFUP), Alameda Professor Hernâni Monteiro, Porto 4200-319, Portugal
[f] Department of Community Medicine, Health Information and Decision (MEDCIDS), Faculty of Medicine, University of Porto, Rua Doutor Plácido da Costa, Porto 4200-450, Portugal

ARTICLE INFO

ABSTRACT

Glioblastoma (GB) is one of the most lethal types of neoplasms with unique anatomic, physiologic, and pathologic features that usually persist after exposure to standard therapeutic modalities. It is biologically aggressive, and the existence of the blood-brain barrier (BBB) limits the efficacy of standard therapies. In this work, we hypothesize the potential of surface-functionalized ultra-small nanostructured lipid carriers (usNLCs) with charge-switchable cell-penetrating peptides (CPPs) to overcome this biological barrier and improve targeted delivery to brain tumor tissues. The big question is: what is the potential of CPPs in directing nanoparticles toward brain tumor tissue? To answer this question, the usNLCs were functionalized with distinct biomolecules [five CPPs, c(RGDfK) and transferrin, Tf] through electrostatic interaction and its ability as a targeting approach to BBB (HBMEC) and glioma cells (U87 cells) evaluated in terms of physicochemical properties, cellular uptake, permeability in a 2D-BBB model, and tumor growth inhibition. Monte Carlo simulations elucidated CPP adsorption patterns. The permeability studies revealed that targeted usNLCs, especially usNLCs[Tf] and usNLCs[CPP4], exhibited an increased permeability coefficient compared to the non-targeted usNLCs. Functionalized usNLCs evidenced enhanced uptake in BBB cells, with smaller CPPs showing higher internalization (CPP1 and CPP2). Similarly, functionalized usNLCs exhibited more significant cytotoxicity in glioma cells, with specific CPPs promoting favorable internalization. Analysis of the endocytic pathway indicated that usNLCs[CPPs] were mainly internalized by direct translocation and caveolae-mediated endocytosis. Optimal usNLCs with dual targeting capabilities to both BBB and GB cells provide a promising therapeutic strategy for GB.

1. Introduction

Brain tumors have a dismal prognosis, and despite the most aggressive treatments available, patients are usually only estimated to live about 18 months after the diagnosis [1]. Physiological barriers, including the blood-brain barrier (BBB), lead to insufficient accumulation of drugs at the tumor site, hampering adequate destruction of tumor cells. [2]. The BBB is a barrier with a unique and organized structure (with tight junction protein complexes, pericytes, astrocytes, and efflux transporters) that (i) acts as a protective shield against pathogens and toxins, (ii) controls the influx and efflux of biological substances (nutrients, ions, or molecules), and (iii) regulates neurotransmitter levels, and consequently brain activity [3,4]. The BBB is permeable to only 2–3% of small molecules (MW < 400 Da and high lipid solubility) and excludes large ones [5]. These properties make the BBB highly selective for drug permeability and present a significant challenge to the transport of drugs to brain tumor tissues.

In this context, nanotechnology can provide a stronger therapeutic response in treating brain tumors and offer a promising solution to this problem [6–8]. Several nanoparticles have been developed to bypass the BBB and treat tumors within the brain. Lipid nanoparticles are a good example of nanoparticles with affinity to BBB due to their lipophilic

---

nature [9–11]. Particularly, ultra-small nanostructured lipid carriers are characterized by a solid-lipid matrix and small particle size (<100 nm), with notable physical stability, biocompatibility and biodegradability, high surface-to-volume ratio, and scale-up potential [12,13]. Moreover, usNLCs can cross the BBB through various transport mechanisms, depending on their specific design and formulation. The surface of usNLCs is easily modified to express individual properties, which allows these particles to cross the endothelial cells of the BBB through transcytosis, such as adsorptive-mediated transcytosis or receptor-mediated transcytosis [14,15]. Active targeting provides advantages in site-specific delivery, reduces off-site drug cytotoxicity, and increases drug accumulation within tumors.

Cell-penetrating peptides (CPPs) and receptor-mediated molecules have been proposed to facilitate drug delivery through biological barriers such as BBB and tumor barriers. CPPs have been widely employed to facilitate the rapid passage of biological materials, offering a promising strategy for transporting large molecules/nanoparticles. This strategy is crucial for treating central nervous system diseases, such as glioblastoma [16–21]. CPPs are small peptides composed of 5–30 amino acids, with the appealing capability of membrane translocation in a nonspecific manner, which relies primarily on adsorptive-mediated transcytosis [22,23]. CPPs can be associated with nanoparticles by electrostatic or covalent interactions, and they are directed across the cell membrane, into the cytoplasm, and to the nucleus. Recent research has explored the use of CPPs as carriers for nucleic acids, small molecule drugs, and nanoparticles to reach the brain [24–29] By binding to specific receptors or proteins, CPPs can actively deliver the cargo to the intended cell at a particular concentration. Despite their potential, CPPs do have limitations. One significant drawback is their lack of targeting specificity, which results in the failure to deliver therapeutic agents exclusively to the desired cells or tissues. However, efforts have been made to enhance the targeting ability of CPPs, such as by modifying their structure or combining them with targeting ligands.

The transferrin receptor (TfR) is overexpressed on the surface of brain capillary endothelial cells and tumor cells in brain tumors, including gliomas [30,31]. TfRs mediate iron accumulation, causing tumor progression and glutamate production, and their overexpression worsens the prognosis for glioblastoma [30]. The fact that TfRs are overexpressed in the BBB and glioblastoma cells can be exploited for the development of targeted nanoparticles against brain tumors [32,33]. Thus, coupling transferrin (Tf) to the surface of usNLCs offers an exciting strategy for particles to overcome the BBB and internalize into glioblastoma cells due to their specificity for TfRs. A receptor-mediated molecule on the usNLCs surface will enable higher specificity, selectivity, and affinity for brain-targeted drug delivery. In turn, tumor-targeting peptides are biomolecules that interact mainly with overexpressed receptors on cancer cells (e.g., c[RGDfK] interacts with integrin receptors).

In this study, the main research question is what role CPPs may play in redirecting nanoparticles into brain tumor tissue. To this end, the usNLCs were functionalized with distinct biomolecules adsorbed on the usNLCs surface, and their ability as a targeting approach to BBB (HBMEC) and glioma cells (U87 cells) was evaluated in terms of physicochemical properties, cell uptake, permeability in the 2D-BBB model, and the tumor growth inhibitory ability. Formulations comprised several targeting strategies, including NPs negatively (uncoated nanoparticles) and positively charged (stearylamine, ST), which were further functionalized with CPPs (CPP1, CPP2, CPP3, CPP4, and CPP5), these imposing variations upon amino acid composition, charge, and molecular weight, and also receptor-mediated molecules such as c[RGDfK], or transferrin.

During the screening process, cell uptake and viability were also immediately assessed to identify targeting strategies more suitable for the effective development of glioblastoma therapy.

2. Materials

Kolliphor® RH40, IR-780 iodide Dye (IR780), and octadecylamine were provided by Sigma-Aldrich (Missouri, USA). Capryol™ PGMC (propylene glycol monocaprylate-type I) and Suppocire® NB were kindly donated by Gattefossé (Gennevilliers, France). Lipoid S 75® (soy phospholipid) was provided by Lipoid GmbH (Ludwigshafen, Germany).

U87 (Human glioblastoma, ATCC® HTB-14) was used for the viability studies. Cell medium (Dulbecco's Modified Eagle Medium, DMEM) and supplements (penicillin-streptomycin, HEPES, and fetal bovine serum) were also acquired from Sigma-Aldrich (Missouri, USA). Human brain capillary endothelial cells (HBMEC) were purchased from Innoprot (Bizkaia, Spain), and the EndroGRO™ MV supplement kit was supplied by Millipore (Massachusetts, USA). EndroGRO™ MV Supplement Kit supplemented with EndoGRO-LS Supplement (0.2%), basal FGF (200 ng/mL), penicillin-streptomycin (1%), L-Glutamine (10 mM), hydrocortisone (1.0 μg/mL), heparin sulfate (0.75 U/mL), ascorbic acid (50 μg/mL) and fetal bovine serum (FBS, 5% v/v).

Ultrapure water (HPLC grade, > 18.2 MΩ was prepared using a Milli-Q water apparatus (Millipore®, Massachusetts, USA) and filtered through a 0.22 μm nylon filter before use. All other reagents and solvents were from analytical or high-performance liquid chromatography (HPLC) grade.

Peptide sequences were produced following the standard Fmoc-SPPS strategy. The Fmoc deprotection was performed using 20% Piperidine in the presence of 0.1 M hydroxybenzotriazole during 3×3 min. The acylation was carried out using 5 eq of amino acids dissolved in DMF together with 4.8 eq O-(1 H-6-chlorobenzotriazole-1-yl), 10 eq N,N-diisopropiletilamina, and 5 eq hydroxybenzotriazole during 2×15 min. Removal of protecting groups was performed using a cocktail mixture containing 95% TFA, 2.5% H_2O, 2.5% TIS during 3 hours. Retention times were acquired by HPLC-DAD analytical system, with a C18 column, using acetonitrile in water with 0.1% trifluoroacetic acid (TFA) as eluent, in gradient mode (10–80%), for 18 minutes, at a flow rate of 1 mL/min and detection at $\lambda = 220$ nm. All peptides showed a degree of purity equal to or greater than 97%.

3. Methods

3.1. usNLCs preparation

usNLCs were produced by hot high-pressure homogenization, as described elsewhere [34]. Briefly, celecoxib (CXB, 5% w/w) and Lipoid® S75 (1%, w/w) were added to the lipid phase (15% w/w), composed of 25:75 Suppocire® NB and Capryol™ PGMC and molten at 50 °C. The lipid phase was subsequently added to 30 mL of a solution of Kolliphor® RH40 (5% w/w) at the same temperature and pre-emulsified (24,000 rpm, 1 min) using a high-speed stirrer (Ultra-Turrax X1020; Ystral GmbH, Germany). The pre-emulsion formed was further processed by hot-high-pressure homogenization for 7.5 min at 1000 bar (Emulsiflex C-3, Avestin, Mannheim, Germany), and the resulting nanoparticles were cooled to 4 °C [34]. Stearylamine (3 mM) was added to the lipid phase to promote a charge reversion to positive values.

IR780 was used as a fluorescent dye to visualize the usNLCs in *in vitro* cellular studies. For preparing fluorescent usNLCs (IR780-loaded usNLCs), 100 μL of an IR780 stock solution (3 mg/mL) in dichloromethane was previously dissolved in the lipid molten phase, followed by the standard procedure above-described. All samples were produced at least in triplicate.

The usNLCs were further purified by ultrafiltration-centrifugation using centrifugal filter units (Amicon® Ultra 4-, Millipore, Germany) with a 50 kDa molecular weight cut-off. 5 mL of usNLCs were placed in the centrifuge filter unit and centrifuged for two cycles of 30 min at 5000 x g and 4 °C. After each purification step, the usNLCs formulations were resuspended in ultra-purified water/PBS. The free drug in the aqueous phase collected in the outer chamber of the centrifuge filter was suitably

diluted in the mobile phase, filtered by a 0.22 μm membrane, and determined by HPLC (as described in section 3.4).

After usNLCs purification by ultrafiltration-centrifugation, different targeting molecules (see the structures in Fig. 1 and respective characteristics in Table 1) were added by electrostatic interaction to negative or positive usNLCs. Transferrin (final concentration of 0.012 mM) or, cell-penetrating peptides (see Fig. 1, in a final concentration of 3 mM), or tumor-penetrating peptide (see Fig. 1, in a final concentration of 8.2 mM) were added to promote different membrane interactions. These are newly synthesized CPPs, not previously tested, and with variations in the positioning and number of lysine, tryptophan, and arginine amino acids. This also imparts variations in size/molecular weight. Table S1 presents the notation used for the different targeted usNLCs formulations, including the respective concentrations.

3.1.1. Colloidal properties

Colloidal properties, specifically, particle size (PS), polydispersity index (PdI), and zeta potential (ZP), were determined by dynamic/ electrophoretic light scattering using a Zetasizer Nano-ZS instrument (Malvern Instruments, Ltd., UK), at 25 °C. Samples were previously diluted 100 times in ultrapurified water and analyzed in triplicate. The results were presented as mean ± standard deviation, extracted from the cumulants algorithm.

3.1.2. Simulation details

3.1.2.1. Model.
Monte Carlo simulations were performed using a coarse-grained model to explore the electrostatic-driven interactions between CPP molecules and the usNLC surface. The CPPs are represented by spring-bead chains described as a sequence of charged and neutral hard spheres connected with harmonic bonds. The chain flexibility is regulated by angular force terms, and the surface of the nanoparticles is represented by hard planar walls with embedded charged hard spheres positioned in the xy plane. The counterions of the CPPs and those of the surface are modeled as hard spheres with monovalent charge. The solvent enters the system through its relative permittivity. Simulations were carried out in the canonical ensemble using the Metropolis algorithm at T = 298 K and ϵr = 78.4 [35]. The long-range electrostatic interactions were handled using the Ewald summation. All particles are enclosed in a box with dimensions $L_x = L_y = 320$ Å, and hard walls are placed at $z_{wall} = \pm 250$ Å. The system is periodic in the x and y directions. A hard sphere radius of 2.0 Å is used for all the species.

The total potential energy, U, of the system can be expressed as a sum of the nonbonded potential energy, $U_{nonbond}$, the bond potential energy,
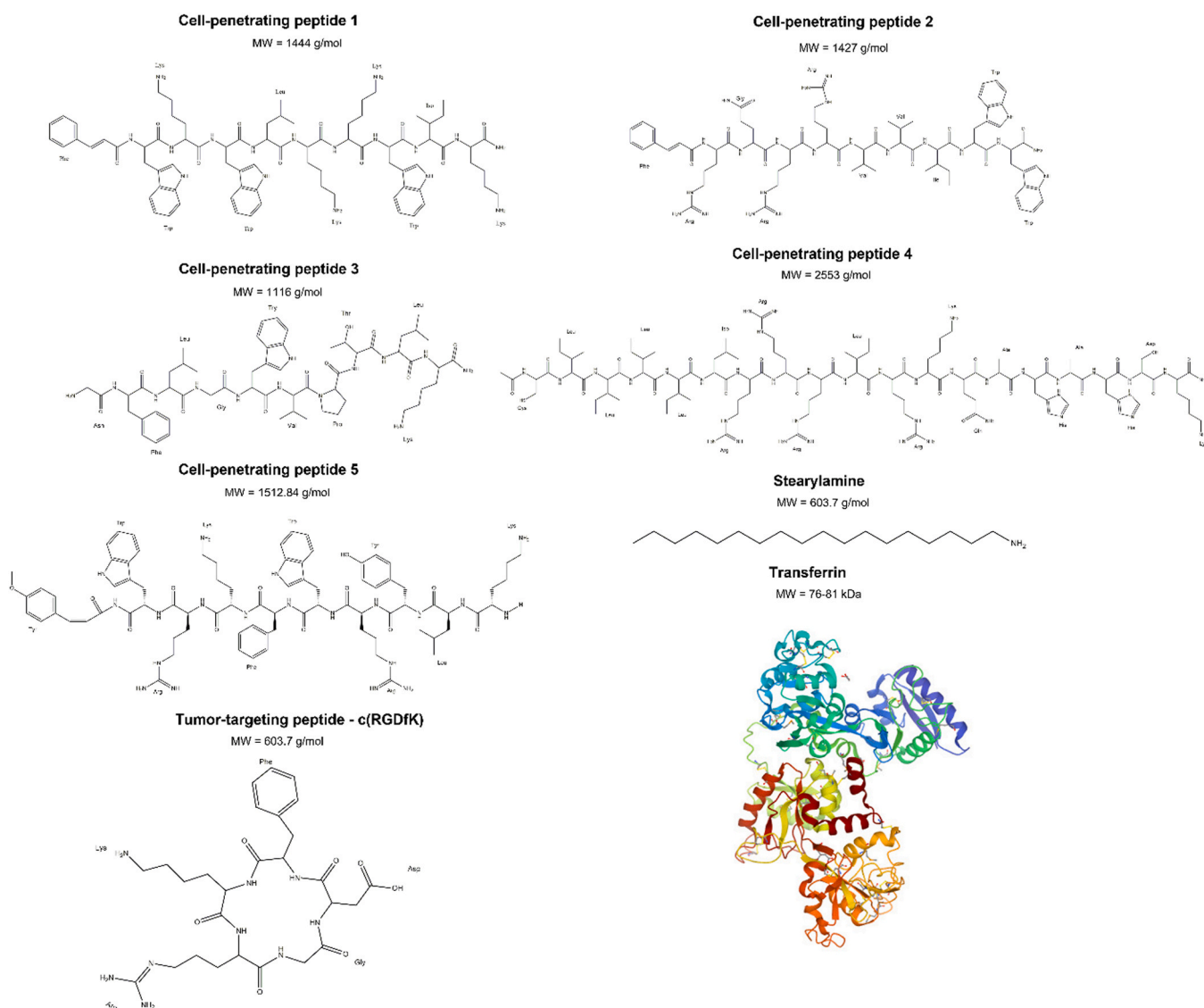

Fig. 1. Molecular structures of cell-penetrating peptides, tumor-targeting peptide, transferrin, and stearylamine used to functionalize usNLCs.

Table 1
Characteristics of the peptides studied in this work.

Code Peptide	Charge*	Sequence	MW	Log P	pI	% Charged residues
CPP1	3	PheGlyTrpLysTrpLeuLysTrpLeuLys-NH₂	1444	3.82	9.54	33
CPP2	4	PheArgGlnArgArgValValIleTrpTrp-NH₂	1427	0.39	12.1	40
CPP3	2	AsnPheLeuGlnTrpValProThrLeuLys-NH₂	1116	-1.27	9.07	25
CPP4	7	CysLeuLeuLeuLeuLeuArgArgArgLeuArgLysGlnAlaHisAlaHisSerLys-NH₂	2553	-10.33	11.8	42
CPP5	5	TrpTrpArgLysPheTrpArgTyrLeuLys-NH₂	1513	3.2	11.2	40
c(RGDfK)	1	c(ArgGly-Asp-d-Phe-Lys)	603.7	-2.96	8.14	67

U_{bond}, the angular potential energy, U_{ang} and the confining external potential energy, U_{ext}. The nonbonded potential energy is given by

$$U_{nonbond} = \sum_{i<j} u_{i,j}(r_{i,j}) \qquad (1)$$

where the summation extends over chain monomers, surface particles, and counterions, with $u_{i,j}$ representing the electrostatic potential plus a hard-sphere repulsion according to

$$u_{i,j}(r_{i,j}) = \begin{cases} \infty, & r_{i,j} < R_i + R_j \\ \dfrac{Z_i Z_j e^2}{4\pi\epsilon_0 \epsilon_r r_{i,j}}, & r_{i,j} \geq R_i + R_j \end{cases} \qquad (2)$$

with Z_i representing the valence of the particle i, R_i the radius of particle i, $r_{i,j}$ the distance between particles i and j, e the elementary charge, and ϵ_o and ϵ_r the permittivity of vacuum and the relative permittivity of the solvent, respectively. Chain monomers are connected by harmonic bonds, and the bond potential energy is given by

$$U_{bond} = \frac{k_{bond}}{2} \sum_{i}^{N_{bond}} (r_{i,bond} - r_0)^2 \qquad (3)$$

being $r_{i,bond}$ the bond length of bond i, r_0 the equilibrium separation, and k_{bond} the force constant (0.4 N m^{-1}).

The angular potential energy, U_{ang}, is given by

$$U_{ang} = \sum_{i=2}^{N_{mon,c}-1} \frac{k_{ang}}{2}(\alpha_{c,i} - \alpha_0)^2 \qquad (4)$$

where $\alpha_{c,i}$ is the angle formed by the vectors $r_{c,i+1} - r_{c,i}$ and $r_{c,i-1} - r_{c,i}$ with the equilibrium angle $\alpha_0 = 180°$ and the force constant $k_{ang} = 3.44 \times 10^{-24}$ J deg^{-2}.

CPPs chains and counterions were not allowed to reside below the surface plane by imposing a confining external potential, for which U_{ext} is given by

$$U_{ext} = \sum_{i} u_{ext}(z_i) \qquad (5)$$

with the summation extending only over chain monomers and counterions with

$$u_{ext}(z_i) = \begin{cases} \infty, & |z_i| > z_{wall} \\ 0, & |z_i| < z_{wall} \end{cases} \qquad (6)$$

CPPs monomers are moved by single-particle translation, full-chain translation, and slithering. The single particle move was attempted 100 times more often than the other two types of moves. The surface particles are fixed, and the counterions are subjected to translational moves. Each simulation started with a random generation of all the system components left to equilibrate by performing at least 5×10^6 trial moves per particle, followed by a production run of at least the same number of moves. CPPs monomers located within 16 Å from the plane of surface charges were considered to be adsorbed. All calculations were performed with the MOLSIM simulation package v.4.0.8 [36].

3.1.2.2. System details. The adsorption of the CPPs was inspected in

surfaces with an overall negative charge density, mimicking the charge of the NP prepared experimentally. According to the zeta potential variation observed with the addition of stearylamine to the usNLCs (as described in section 4.1.), an overall charge density of 9.4×10^{-3} C/m^2 was estimated for each NP. In the model, the NP surface comprises 64 negatively charged hard spheres regularly distributed in a square grid, with the closest distance between charges of 40 Å. Each CPP molecule was modelled by sequences of neutral and positively charged hard-spheres according to the scheme presented in Table 2.

3.1.3. Stability studies

Assessing the physical stability of usNLCs includes supervising the presence of particle aggregation, which may lead to sedimentation or creaming phenomena, dependent on temperature and storage time. Lipid modifications might also change the structure of the usNLCs, influencing the loading and release capability and, consequently, the *in vivo* performance. Therefore, the effects of size control and NPs growth are important for preparing dispersions, and particular attention must be given to their evolution.

The optimized usNLCs formulation was studied for stability at 4 °C, 25 °C, 37 °C, and 40 °C simulating the fridge, room temperature, accelerated testing, cell medium, and human plasma as described in Table S2. The stability studies were conducted according to the method reported previously [37].

3.1.3.1. Long-term storage stability. The long-term storage stability of usNLCs was investigated by analyzing the change in particle size, PDI, and ZP after storage at different temperatures. For this purpose, 2 mL vials carrying samples of usNLCs were kept at freezing temperature (4 °C), room temperature (~25 °C), and accelerated testing temperature (40 °C). Samples were analyzed at predetermined time intervals (see Table 4) and checked for several physicochemical parameters to judge the storage stability of usNLCs. These included particle size, PdI, and zeta potential, which were considered quality parameters.

3.1.3.2. In vitro pH stability of usNLCs formulations. Each buffer solution was added to the usNLCs formulations (diluted six times) and incubated for 2 hours at 37 °C before measurements. After diluting 100 times with ultrapurified water, the samples were analyzed three times. The stability of the optimized usNLCs formulations was studied considering the following parameters: particle size, PDI, and ZP after incubation in different pH solutions (5.5 and 7.4).

3.1.3.3. Cell medium stability. The influence of cell culture medium on usNLCs formulations was also addressed. The usNLCs were dispersed in

Table 2
Summary of the characteristics of the model representing each CPP.

Label	Overall chain charge	Model	Number of chain monomers
CPP1	+5	00+00++00++	11
CPP2	+5	++++00000+	10
CPP3	+2	+00000+	7
CPP4	+7	0000+++0+++000+	15
CPP5	+5	00++00+00++	11

cell culture medium (1:1) and subsequently incubated at 37 °C for 24 and 72 hours, the time points used for *in vitro* cytotoxicity studies. Finally, usNLCs were tested by evaluating the mean particle size, PdI, and ZP of usNLCs.

3.1.3.4. Protein adsorption study. The stability of usNLCs in serum proteins was considered to infer the effect of protein adsorption on the colloidal properties of NPs when they come into contact with plasma proteins after *in vivo* administration [38]. For this purpose, usNLCs were dispersed in PBS solution (1:1 v/v) of pH 7.4 and mixed with a 1% albumin protein solution. After shaking at 37 °C for 2 hours at a speed of 100 rpm, aliquots were taken out to measure protein adsorption by analyzing particle size, PdI, and ZP changes.

3.1.3.5. Serum stability. The effect of the usNLCs formulations on serum stability was analyzed regarding mean PS, PdI, and ZP in the presence of bovine serum. The usNLCs preparations were diluted with fetal bovine serum (FBS, 1:1 v/v), and the mixture was then incubated at 37 °C under mild stirring for 2 hours.

3.1.3.6. Plasma stability. Plasma samples were collected from female mice. Next, the usNLCs formulations were incubated with the same plasma volume (1:1 v/v) at 37 °C for 2 hours. 100 μL of the samples were taken and examined further for particle size, PDI, and ZP changes.

3.2. In vitro studies in HBMEC

3.2.1. Cytotoxicity assay

Cells were cultured at 37 °C and 5% CO_2 in flasks coated with 0.3 mg/mL rat tail collagen type I (BD Biosciences) for 1 hour at 37 °C. The flask was changed every 3–4 days when cells were approximately 90% confluent. HBMEC between 2 and 15 passages were used in all studies.

To ensure that the usNLCs did not disrupt the barrier due to toxicity, a safe usNLCs dose was established using the cell proliferation assay before the permeability assay. Freshly prepared usNLCs were passed through 0.2 μm filters and transferred to sterile 2 mL tubes before cell culture experiments. 20×10^3 cells/well were seeded in a 96-well plate and incubated at 37 °C and 5% CO_2 for 24 hours. The cytotoxicity of nine different loaded-usNLCs was tested using an increasing concentration (0–2500 μg/mL lipid content) for 4 and 24 hours. The resazurin assay was used to determine the cytotoxicity of usNLCs. Accordingly, 100 μL of 10% (w/v) resazurin solution in EndroGRO™ medium was added to the cells and incubated for approximately 2 hours at 37 °C. The enzymatic reduction of resazurin to resorufin was analyzed by UV/Vis spectrophotometry at 570 nm and 600 nm. Cell viability was assessed indirectly according to

$$\%Cell\ Viability = 100\ \ x\ \ \frac{(Abs_{570nm} - Abs_{600nm})_{Treated\ Cells}}{(Abs_{570nm} - Abs_{600nm})_{Control}}$$

3.2.2. Permeability studies through the blood-brain barrier

Cells between 2 and 15 passages were grown in EndoGRO™ medium. An *in vitro* model of the BBB was established. Cells (5×10^4 cells/cm^2) were seeded on the apical side of transwell inserts (in 6-well collagen pre-coated Transwell®, 0.4 μm pore PTFE membrane insert, Corning Life Sciences) and grown for 7 days at 37 °C and 5% CO_2. Medium (1.5 mL in the apical compartment and 2.6 mL in the basolateral compartment) was changed every 2–3 days. The formation of tight junctions (TJ) was monitored by measuring the transendothelial electrical resistance (TEER) of the cell monolayer by using an EVOM resistance meter (World Precision Instruments, Hertfordshire, UK), the TEER values should be between 120 and 150 Ω.cm^2 [39,40].

On day 7 of HBMEC culture in the transwell system, CXB-loaded usNLCs (20 μg/mL of CXB concentration, 0.4 mg/mL of lipid content) suspended in the fresh medium were added to the apical compartment of the transwell. After 0.5, 1, 2, and 4 hours, the medium in the lower chamber was collected and analyzed by HPLC for CXB determination (as described in Section 3.4.). The initial amount of CXB added to the upper compartment was considered the total CXB, and the amount of CXB permeated was presented as the percentage of this initial quantity. The amount of CXB measured in the medium collected from the lower chamber was expressed as a percentage of CXB in the upper chamber at zero time. The same procedure was carried out in empty transwell inserts to understand if the artificial membrane by itself compromises the passage of usNLCs. Permeability under steady-state conditions can be evaluated mathematically by the apparent permeability coefficient, P_{app}, according to

$$P_{app} = \ \ \frac{dQ}{dt}\ \ \frac{1}{AC_0}$$

where dQ/dt is the solute flux (μg/s) across the barrier, A is the surface area of the transwell (cm^2), and C_0 is the initial donor concentration (μg/mL) [41].

At the end of the experiment, the permeability of the highly hydrophilic and low molecular weight Lucifer yellow (LY, 457 Da) was calculated to confirm the membrane's integrity after the experiment, as previously described by [42,43]. The culture medium was removed, and cells were washed twice with PBS before adding 20 μM LY in the upper chamber for 1 hour. The amount of LY in the lower chamber was measured fluorometrically from 200 μL collected at 0, 20, 40, and 60 min at the excitation and emission wavelengths of 485 nm and 535 nm.

3.2.3. Cell uptake assay

The cellular uptake in HBMEC of free IR780 and IR780-labeled usNLCs was assayed by flow cytometry (ACEA NovoCyte® ACEA Biosciences, Inc.). 0.5 mL of cell suspension with 20×10^3 cells/well were seeded 24 hours before the experiments into 24-well tissue culture test plates. IR780 was used as a fluorescent probe to investigate the cellular uptake of nine different usNLCs. IR780 (peak emission at 780 nm) is a heptamethine cyanine dye with higher fluorescence intensity and superior stability than the clinically approved dye (*e.g.,* Indocyanine green, ICG). At 200 μg/mL of lipid content, the samples were added and incubated for 0.5, 1, 2, and 4 hours at 37 °C in 5% CO_2. Free IR780 was removed from usNLCs by filtration using centrifugal filter devices (Amicon® Ultra, Ultra cell-50k, Millipore, USA). The control group was treated following the same steps without usNLCs. After incubation, the cells were washed three times with cold PBS to remove the non-internalized usNLCs and trypsinized. Then, cells were centrifuged at 1500 x g for 5 min and fixed with 4% paraformaldehyde for 30 min at room temperature. Cells were once again washed with PBS, centrifuged, resuspended in PBS, and analyzed through flow cytometry, using a 640 nm laser for excitation of IR780 and 780/60 nm for detection of IR780.

3.2.4. Internalization pathways

Identification of specific endocytic processes involved in the complex internalization of usNLCs was done through a cellular uptake study in the presence of inhibitors of each pathway. All the inhibitors were used to maximize the effects of the compounds while minimizing their inherent toxicity. The pathways involved in the internalization of usNLCs on BBB were studied by pre-incubating HBMEC cells in 24-well plates (20×10^3 cells/well) with different inhibitors for 30 min (see Table 3). Cells were then incubated with IR780-labeled usNLCs (0.01 μg/mL IR780) for 2 hours and, after that, were washed twice with PBS, detached with 0.25% trypsin−EDTA, and the internalization of usNLCs analyzed by flow cytometry as described above. The acquisition process involved gating cells based on forward *vs.* side scatter to remove dead cells and debris. Subsequently, 10,000 gated events were recorded for every sample. The results were compared with those of cells

Table 3
Summary of chemical endocytosis inhibitors [44–47].

Pathway	Inhibitor	Classical size of endocytic vesicle	Mechanism
Endocytosis	Low temperature (4 °C)	-	Blocks energy-dependent process
Clathrin-mediated endocytosis	Sucrose (0.45 M)	~100 nm	Inhibits clathrin-mediated endocytosis
Caveolae-mediated endocytosis	Filipin (1 μg/mL)	60–80 nm	Inhibits lipid raft/caveolae-mediated endocytosis
Phagocytosis or Macropinocytosis	Cytochalasin B (1 μg/mL)	>200 nm	Depolymerises the actin filaments, avoiding the formation of the structures essential to enclose particulates

incubated without inhibitor.

$$\%Inhibition = 100 \; x \; \frac{Fluorescence_{Control} - Fluorescence_{Inhibitor}}{Fluorescence_{Control}}$$ where, Fluorescence$_{Inhibitor}$ and Fluorescence$_{Control}$ refer to the fluorescence measurements in the presence and absence of inhibitors, respectively.

3.3. In vitro studies in U87 cells

3.3.1. Cytotoxicity assay
U87 cells were cultured in DMEM medium, supplemented with 10% (v/v) FBS, 1% (v/v) penicillin-streptomycin solution, and sodium bicarbonate. Cells were maintained at 37 °C in a humidified atmosphere containing CO_2 (5%). Briefly, 20×10^3 cells/well were seeded in a 96-well plate and incubated for 24 or 72 hours after replacing the medium with increasing concentrations of usNLCs formulations. Subsequently, the medium was removed, and the cell viability was determined by resazurin assay, as described above.

3.3.2. Cell uptake assay
The cellular uptake in U87 cells of free IR780 and IR780-labeled usNLCs was assayed by flow cytometry (ACEA NovoCyte® ACEA Biosciences, Inc.). For that, 0.5 mL of cell suspension with 20×10^3 cells/well were seeded 24 hours before the experiments into 24-well tissue culture test plates. At 400 μg/mL of lipid content, the samples were added and incubated for 1, 2, 4, and 8 hours at 37 °C in 5% CO_2. Note that a more prolonged exposition time was used to inspect potential discriminatory effects regarding uptake behavior. IR780 was removed by filtration using centrifugal filter devices (Amicon® Ultra, Ultra cell-50k, Millipore, USA). The control group was treated following the same steps without usNLCs. After incubation, cells were washed three times with cold PBS to remove the non-internalized usNLCs and trypsinized. Then, cells were centrifuged at 1500 x g for 5 min and fixed with 4% paraformaldehyde for 30 min at room temperature. Cells were once again washed with PBS, centrifuged, resuspended in PBS, and analyzed through flow cytometry (ACEA NovoCyte®, ACEA Biosciences, Inc., USA). The acquisition process involved gating cells based on forward vs. side scatter to remove dead cells and debris. Subsequently, 10,000 gated events were recorded for every sample. A 640 nm laser for the excitation of IR780 and 780/60 nm for detecting IR780 were used.

3.3.3. Internalization pathways
The pathways involved in the internalization of functionalized and non-functionalized usNLCs on glioblastoma were studied by pre-incubating U87 cells in 24-well plates (20×10^4 cells/ well) with different inhibitors for 30 min, as referred to in section 3.2.4 and Table 3. Cells were then incubated with IR780-labeled usNLCs (1.80 μg/mL IR780) for 2 hours, washed twice with PBS, detached with 0.25% trypsin−EDTA, and the internalization of usNLCs analyzed by flow cytometry as described above. The results were compared with those of cells incubated without inhibitor.

3.4. Instrumentation and chromatographic conditions

The HPLC analysis of CXB was carried out using a Shimadzu LC-2010 C HT apparatus (Shimadzu Co., Kyoto, Japan) equipped with a quaternary pump, a CTO-10AS oven, and an SPD-M2OA detector. A Kinetex® EVO C18 column (Torrance, USA), with 5 mm particle size, 4.6 mm internal diameter, and 150 mm length, was used for the analysis in an oven at a temperature of 35 °C. Chromatographic analysis was conducted in an isocratic mode. The mobile phase consisted of a mixture of glacial acetic acid (2% v/v): acetonitrile of 55:45 (v/v) and at a constant flow rate (1.2 mL/min) [48]. A run time of 13 min was established, and celecoxib was eluted at 11.1 min. The detection was carried out at 250 nm, and an injection volume of 10 μL was used for all standards and samples. A stock solution was first prepared, followed by the calibration standards, and quality controls containing the analyte were subsequently obtained. The results were processed using Shimadzu LC-solution version 1.12 software.

3.5. Data analysis

All experiments were performed in triplicate. The total lipid content of the particles reflecting a 50% reduction in cell viability (IC$_{50}$) was calculated from concentration-response curves, with the sigmoidal curve fitting method, using Prism version 8 (GraphPad Software, Inc., USA). One-way ANOVA ($\alpha = 0.05$) with Tukey's multiple comparisons was used for assessing the statistical significance of factors pertaining to physicochemical characteristics and in vitro cellular performance. A t-test was considered to evaluate the statistical significance of each inhibition condition.

Further analysis, based on unsupervised machine learning methods [13,25,49,50], including Hierarchical cluster analysis (HCA) and principal component analysis (PCA), was performed using JMP Pro 16.0.0 software (SAS Institute Inc.) to infer the influence of the physicochemical properties of the targeting molecules on the usNLCs surface on the cell interaction (HBMEC vs. U87).

4. Results and discussion

4.1. Surface functionalization

The major obstacle in brain drug delivery is crossing the BBB. This work aimed to obtain a usNLCs formulation with suitable particle size, morphology, and targeting ability for efficient brain delivery. To achieve this goal, different approaches were considered to assign usNLCs (i) a positive charge and (ii) functionalization with active targeting molecules without compromising the small particle size.

Stearylamine was added at a concentration of 3 mM (usNLCsST), and the zeta potential was reverted to positive values (from -27±4 to +34 ± 5 mV). Although the positive charge promotes increased cellular uptake, stearylamine is not a targeting molecule for cells, having an affinity with any negatively charged membrane [51]. The positive charge also increases the probability of protein corona formation due to the absorption of anionic serum proteins, contributing to rapid clearance and decreasing the circulation half-life [52].

For these reasons, changing nanoparticle properties, such as surface chemistry using biorecognized molecules, may alter the protein corona composition or block the nonspecific protein adsorption on nanoparticles [53,54]. Several studies support that those biomolecules diminish interaction with serum proteins and increase blood residence time. Moreover, the nanoparticle surface modification with biomolecules seems to be a significant step in targeting a specific barrier (e.g., BBB or BTB) [21]. Active targeting molecules such as cell-penetrating peptides, proteins, or tumor-targeting peptides were used to functionalize the nanoparticle surface, and their performance was evaluated in

terms of stability in biological fluid and targeting ability to biological barriers (BBB or BTB). Functionalized-usNLCs were prepared by surface charge interaction (electrostatic interaction) between usNLCs/usNLCsST and active targeting molecules (Table 2). Molecules with a negative charge (at pH 6.6) were added to usNLCsST (as Tf), and the positively charged peptides (at pH 6.6) were added to usNLCs (CPP1, 2, 3, 4, 5, and c[RGDfK]). Based on previous results, the concentration of cell-penetrating peptides (CPP1, 2, 3, 4, and 5) was determined considering the amount of stearylamine (3 mM) [25,50]. The concentration of c(RGDfK) (8.28 mM) and Tf (0.012 mM) was established based on different studies already published [55–58]. Table 4 summarizes the colloidal properties of the formulations, including particle size, zeta potential, and polydispersity index. usNLCs were characterized by sizes around 59–70 nm and a polydispersity index below 0.2. The surface modification did not affect size but impacted the zeta potential. The interaction between biomolecules and usNLCs/usNLCsST explains changes in the latter. The addition of Tf reverted the usNLCsST ZP from +34 to −17 mV; CPP1, CPP4, and CPP5 also reverted the usNLCs ZP value; CPP2, and c(RGDfK) displayed a ZP value increased to zero. Purified nanoparticles exhibited a final CXB concentration of 5.18 ±0.24 mg/mL for usNLCs and 4.61±0.09 mg/mL for usNLCsST. Following the physicochemical characteristics, formulations were further inspected regarding stability and biosafety behavior in two cell lines (HBMEC and U87 cells).

4.1.1. Monte Carlo simulation

In order to clarify the surface modifications of the usNLCs upon CPP adsorption, namely the extent and the patterns of chain adsorption, Monte Carlo simulations were performed, employing a simple model, as illustrated in Fig. 2 A. The idea was to reduce the inherent complexity of these systems, focusing on a small set of parameters (overall chain charge, chain length, and charge distribution) in order to assess their impact on the overall behavior of the systems. Five different systems were considered, as described in section 3.1.2. The analysis aimed to elucidate the degree of CPP adsorption to the NP surface and the conformational behavior of each CPP molecule upon adsorption.

The adsorption profile of the CPP chains was assessed by the probability density of each particle type along the z-axis (Fig. 2 B). Their conformation was evaluated by the data presented in Table 5, which includes the values of the radius of gyration, R_g, end-to-end distance, R_{ee}, and the number (N), and length (L) of trains, tails, and loops of the CPP chains upon adsorption according to the scheme represented in Fig. 2 C. The adsorption of each chain was obtained by the number of adsorbed segments, n_{train}. The results presented in Fig. 2 B show the preferential positioning of the chains near the surface, clearly confirming the stability of the electrostatic interaction between the CPP

molecules and the surface of the usNLC. The plot points out a lower adsorption of the CPP4 molecule in comparison with the other CPPs. Also evident is the similar behavior of CPP1 and CPP5, whose density profiles are perfectly overlapped. According to this analysis, the CPP3 molecules have a broader distribution along the z-axis, suggesting a weaker interaction with the surface. Looking at the results presented in Table 5, it can be seen that the number of adsorbed monomers in each chain (n_{train}) follow the order CPP1=CPP5>CPP2>CPP4>>CPP3. This trend and the z-density profiles clearly confirm the zeta potential values obtained for these systems. In fact, according to these results, it would be expected that a higher variation in zeta potential would occur for CPP1 and CPP5. This is confirmed experimentally by the zeta ZP values obtained (see Table 4). The comparison between CPP2 and CPP4 reveals that while CPP4 exhibits lower adsorption compared to CPP2, the higher charge of the CPP4 molecule still results in a similar ZP value alteration observed in the system containing CPP2 molecules. Finally, CPP3 showed a looser interaction with the NP surface, as confirmed by both Z-density profiles and n_{train} values. This weaker interaction and its lowest overall charge lead to the smallest ZP variation experimentally observed. Regarding the conformational behavior of the different CPPs upon adsorption, it can be seen that, generally, the number and length of trains are higher than that of loops and tails. This suggests a higher preference for the chains to attach to the surface instead of being hanged on the surface. The exception occurs for CPP4, in which the length of the tails is higher than that of the trains. Noteworthy is the fact the molecules with similar chain lengths and the same overall charge (CPP1, CPP2, and CPP5) present different adsorption behaviors due to their different charge distribution along the chain. The higher charge concentration on one side of the chain in CPP2 does not induce stronger electrostatic-driven adsorption. In fact, a more uniform distribution of the charged groups along the backbone, as occurs in CPP1 and CPP5, seems to favor the electrostatic interaction with the NP surface.

The spatial distribution of the different CPP molecules on the NP surface was also evaluated by resorting to positioning density maps, presented in Fig. 2 D. The plots contain the probability of finding a selected charged segment of the chain at each point of the surface, relative to that found in a uniform distribution. It can be seen that despite the low surface charge density of the nanoparticles, their surface coverage is generally almost uniform. This is consistent with the estimates depicted in Table 4.

4.1.2. Stability studies

Evaluating the stability of formulations is essential for quality assurance. Thus, warranting the state of dispersion throughout the product lifecycle is a challenge due to the dynamics associated with the dispersions. Besides PS, PdI, and ZP as usNLCs quality control parameters, the stability of the dispersion should be assessed in biological media. In biofluids, usNLCs formulations rapidly become enclosed by a protein corona (PC). Thus, it is important to understand the interaction between the usNLCs surface and the fluid interface. In some studies, the formation of PC has been described as dependent on the interplay of competition between different proteins for the location near the nanoparticle-solution interface. This adsorption of proteins is accompanied by reconfiguration of their native structure, also known as denaturation [61]. In general, the formation of PC is thought to minimize the specific targeting of NPs and to form a separation between the targeting ligands and their surrounding medium. Some studies claim that the optimal surface charge of NPs designed for *in vivo* application should be close to neutral to increase circulation time, enhance tissue penetration, and avoid the reticuloendothelial system. This is an important finding in increasing passive retention in tumors [62]. The PC formation or particle aggregation significantly interferes with the *in vitro* (NPs uptake or cytotoxicity) and *in vivo* behavior (pharmacokinetics and toxicity). Therefore, identifying the factors responsible for NPs colloidal stability and aggregation is clearly relevant [63]. Understanding how NPs properties and, more importantly, colloidal behavior in biological

Table 4

Physicochemical characteristics, including particle size (PS), polydispersity index (PdI), and zeta potential (ZP) of purified CXB-loaded usNLCs formulations. Data are expressed as mean ± SD (n = 3, ** $p<0.01$ and **** $p<0.0001$ usNLCs *vs.* functionalized-usNLCs).

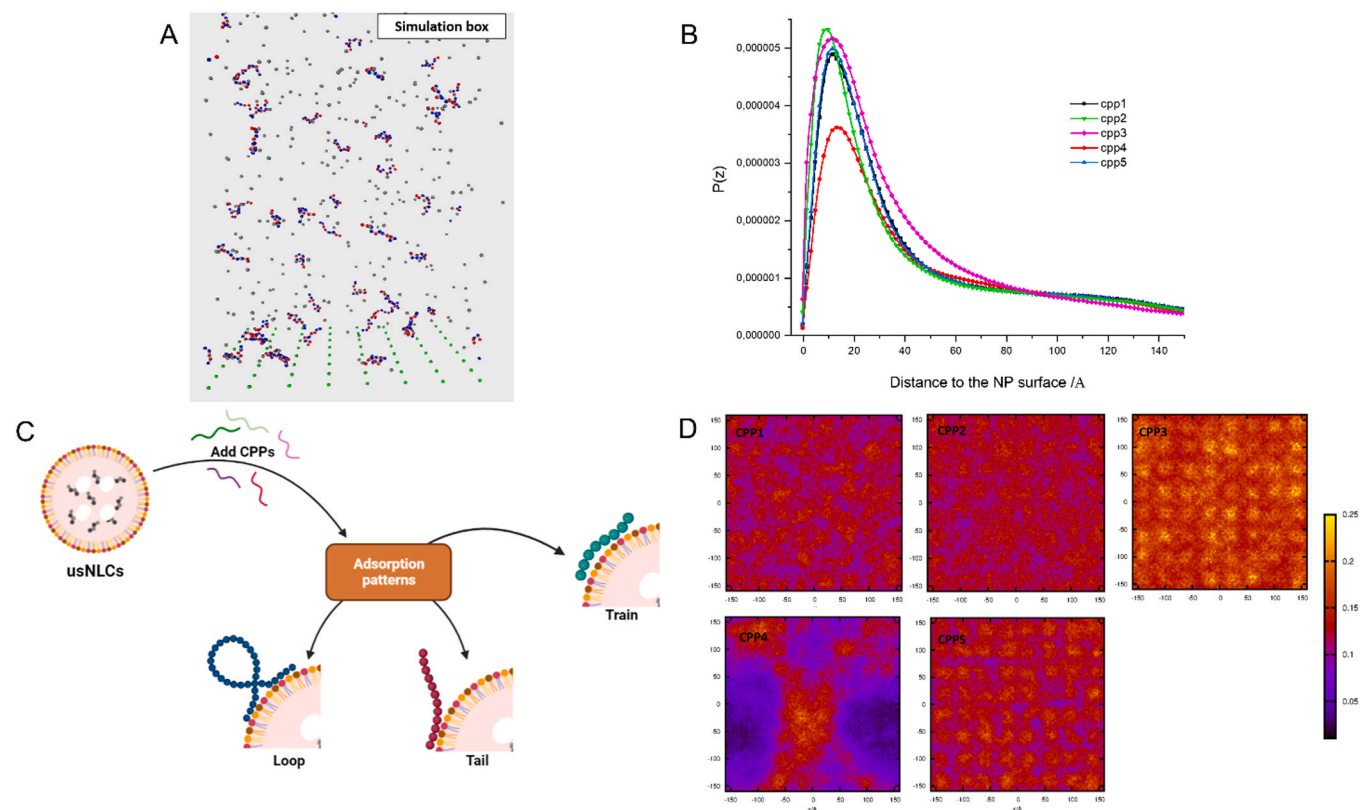| Formulations	PS (nm)	PdI	ZP (mV)	Molecules per NP (x10^{-10}) [59,60]
usNLCs	65.1 ±0.3	0.168	-27±4	-
usNLCsST	70±3	0.100	34±5****	-
usNLCs^{Tf}	61±1	0.100	-18±2**	-
usNLCs^{CPP1}	59±2	0.118	17±1****	5.52
usNLCs^{CPP2}	65±5	0.102	-1.2 ±0.3****	5.44
usNLCs^{CPP3}	59±1	0.087	-18±3**	4.33
usNLCs^{CPP4}	67±2	0.154	2.5±0.2****	5.52
usNLCs^{CPP5}	58±2	0.093	16.2 ±0.4****	5.36
usNLCs^c (RGDfK)	59±2	0.195	-5±2****	-

Fig. 2. A) Computational design of the system. Illustration of the coarse-grained model with the CPP represented by the red-blue chain and the surface of the NP modeled by a hard-planar wall with negatively charged particles (green) regularly distributed in the xy plane. Gray spheres represent the surface and the CPP counterions. B) Probability density profiles, along the z-axis, for each CPP chain, considering that the usNLC surface is positioned at z=0. C) Schematic representation of the different adsorption patterns, trains (sequences of adsorbed monomers), tails (sequences of non-adsorbed monomers), and loops (sequences of non-adsorbed monomers between trains). D) Positioning density maps of a monomer representative of each CPP chain.

Table 5
Values for the conformational parameters of CPPs that characterize the adsorption patterns of each type of chain.

CPP	R_{ee}/Å	R_g/Å	N_{train}	N_{tail}	N_{loop}	L_{train}	L_{tail}	L_{loop}	n_{train}
CPP1	27.97	10.64	0.258	0.150	0.057	5.416	4.623	2.186	1.398
CPP2	26.20	9.87	0.256	0.140	0.052	5.242	4.247	2.057	1.365
CPP3	18.62	7.36	0.257	0.134	0.033	4.439	2.811	1.647	1.141
CPP4	35.65	13.60	0.226	0.149	0.065	5.868	6.209	2.648	1.328
CPP5	28.06	10.66	0.259	0.150	0.057	5.397	4.675	2.184	1.396

solutions (*e.g.*, cell culture media or body fluids) impact cellular interactions and cell responses is critical. Thus, different pHs (physiological and tumor pH), cellular medium, albumin, mouse plasma, or FBS were used as fluids to test the stability of the usNLCs. The usNLCs were incubated in different buffers (United States Pharmacopeia, USP), including pH 7.4 and 5.5, and the results are shown in Table S3. usNLCs were dispersed appropriately without significant differences in PS and PdI. However, ZP values decreased, except for usNLCs, due to the deprotonation of amine groups (see structures in Fig. 1).

The stability in albumin, FBS, or mouse plasma (see also Table S3) was additionally evaluated, with diverse results. The usNLCs incubated with albumin and FBS did not show significant differences in PS and PdI, except for usNLCsST. This fact can be explained by the high positive ZP value, which leads to the adsorption of various proteins present in these media. In turn, usNLCs incubated with mouse plasma significantly modify PS, PdI, and ZP (Table S3). usNLCs and usNLCsST, without a stealth coating, attract proteins present in this medium, increasing the particle size (> 1000 nm) and neutralizing the ZP. At the same time, when the formulations are incubated with mouse plasma, there is a significant shift in the ZP to neutral values, regardless of

functionalization. Predictably, there were no PdI values below 0.350 in mouse plasma, which means aggregation between nanoparticles occurred after PC formation. Fig. 3, summarizes in three "spider charts" the effect of albumin, FBS, and mouse plasma on the physicochemical properties (PS, PdI, and ZP, respectively) of nine usNLCs (non-functionalized and functionalized).

The usNLCs interact with the cell culture medium components (serum albumin, ionic salts, and amino acids), which leads to loss of surface functionality and subsequent slight aggregates, therefore affecting their performance *in vitro/in vivo*. For example, the total protein levels in the cell culture medium are approximately 20 times less than the protein content in the human/mouse plasma. Thus, the dispersion of usNLCs in the cell media is important to understand how the NPs are presented to cells. Phenomena such as aggregation or charge loss of the NPs in the assay medium would indicate a reduction of the available NPs. To evaluate the effect of the cell culture medium, usNLCs were incubated *in vitro* at 37 °C in the presence of DMEM and EMEM in order to simulate the cell culture conditions (different incubation times, 4, 24, and 72 hours) and the PC formation. Incubation of usNLCs with the cellular medium after 4 hours and 24 hours showed no differences.
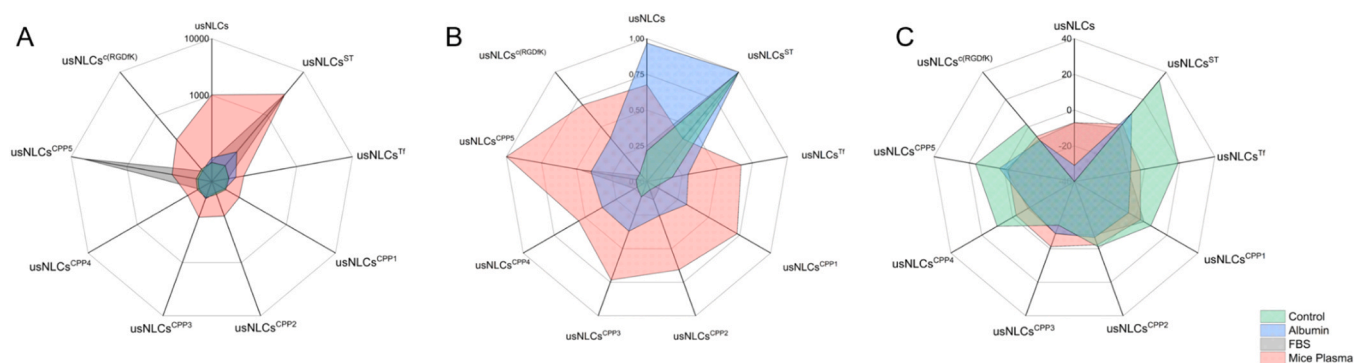
Fig. 3. "Spider chart" summarizing the different physicochemical properties of non-functionalized and functionalized nanoparticles in the most relevant media (control – green; albumin – blue; FBS – gray and mouse plasma - red): (A) particle size, (B) PdI, and (C) zeta potential. Key: Tf - transferrin; CPP – cell-penetrating peptides; PS – particle size; PdI – polydispersity index; ZP – zeta potential; FBS – fetal bovine serum. 4.2. *In vitro* studies in HBMEC cells.

However, at 72 hours, PS was statistically different for usNLCs, usNLCsST, and usNLCs^{CPP5}, exhibiting values above 100 nm (for PS) and 0.250 (for PdI). The ZP changed considerably for all the formulations, which is explained by the affinity of proteins present in the cell medium and by the deprotonation of amine groups in the cell culture medium (pH 7.4). The ZP of usNLCsST changed markedly from +34±5 mV to -14 ±1 mV.

Some general conclusions could be drawn from these studies about the colloidal stability and the PC formation: (i) usNLCs formulations were stable at different pH and albumin content, with a slight variation in ZP values (mainly in the presence of amine groups); (ii) usNLCs without a stealth coating showed the worst stability in FBS, cell medium, or mouse plasma; this can compromise the intravenous administration and the prolonged circulation half-life, being rapidly cleared by the reticuloendothelial system; (iii) in contrast, functionalized-usNLCs are less prone to fluctuations than non-functionalized usNLCs, suggesting that protein adsorption was decreased, or not observed when the usNLCs are coated with CPPs; and (iv) neutral and negatively charged nanoparticles reduce the plasma protein adsorption, which results in longer blood circulation time than positively charged nanoparticles.

The long-term storage stability of usNLCs was assessed, and parameters are displayed in Table S4. The results indicate that usNLCs were stable over one year at 4 °C and room temperature, while usNLCsST were stable over nine months at 4 °C and room temperature. ZP was the most variable parameter over time, irrespective of the formulation. Despite this, it remained within the acceptable range for anti-cancer drug delivery. This result suggests appropriate colloidal stability of all the formulations, even at room temperature. However, usNLCs and usNLCsST were not stable at temperatures around 40 °C for prolonged periods. This instability may be justified by the presence, in the lipid matrix, of a solid lipid with a melting point lower than 40 °C, affecting all analyzed parameters (PS, PdI, and ZP). Similar results for the functionalized-usNLCs stored at 4 °C were obtained. The PS and PdI were stable over time. PS and ZP changed substantially even after nine months, and it was comparatively higher than the T$_0$ point data. ZP, however, changed, having been reversed in the case of usNLCs^{Tf} (-18±2 mV switched to 23 ±3 mV, after 9 months), usNLCs^{CPP1} and usNLCs^{CPP2} (17±1 mV switched to -11±1 mV and 11±1 mV switched to -10±1 mV, respectively), see Table S4.

4.2. In vitro studies in HBMEC cells

4.2.1. Cytotoxicity studies

The blood-brain barrier (BBB) is mainly composed of brain capillary endothelial cells connected through intermolecular tight junctions, which regulate cellular functions and protect the brain from exogenous and endogenous substances. Therefore, overcoming the BBB is a critical obstacle for most therapeutic molecules to enter into the brain tissue,

resulting in lower accumulation in the brain. The BBB expresses some receptors and carriers that can facilitate the transport with the help of specific ligands. Simultaneously, the BBB membrane is negatively charged and exhibits a high affinity for positively charged compounds. Both strategies could trigger internalization and help to cross the BBB [23].

This study intended the development of NPs with a size <100 nm that would allow passive diffusion through the BBB [23]. In addition, several molecules used as active targeting strategies were investigated. To shorten the usNLCs permeation through the BBB, receptor-mediated transport (addressing transferrin receptors expressed on the BBB) and adsorptive-mediated transport (addressing the interaction of cell-penetrating peptides with BBB) were the two strategies addressed in this work. To this end, the permeation study of usNLCs through the HBMEC cell monolayer, adopted as an *in vitro* model of the BBB, was performed to select the molecule or molecules with the best penetration rate.

Before conducting the permeability studies, the potential cytotoxicity of the usNLCs was investigated in the HBMEC (Fig. 4 A). CXB-loaded usNLCs were suitably dispersed in cell media, and their cytotoxicity was investigated. As expected, the IC$_{50}$ at 4 hours was higher than the IC$_{50}$ at 24 hours (see Fig. 4 A). At 4 hours, usNLCs had the same behavior, with no significant differences between the formulations as extracted from one-way ANOVA. However, the decrease in IC$_{50}$ at 24 hours was more pronounced for usNLCs, usNLCsST, usNLCs^{Tf}, and usNLCs^{CPP4}, with significant differences between time points. The cytotoxicity of stearylamine could be explained by its high zeta potential (+ 34±5 mV) in water. However, as shown in Table S3, the zeta potential of usNLCsST reverted to negative values due to the deprotonation of amine groups at pH 7.4. As previously mentioned, the nanoparticles are introduced into a biological medium and adsorb proteins on their surface, forming a new interface. For this reason, the cytotoxicity associated to the stearylamine nanoparticles may not be directly associated to positive charge but with the chemical structure, as explained in Mendes *et al.* [64]. The cytotoxicity profile of the cationic surfactants studied depended on the alkyl chain tail length. Human Tf and different CPPs, composed of natural amino acids, have been chosen for lower toxicity and bio-interaction with receptors and membranes. These structures overcome the negative impact of commercial cationic lipids (stearylamine), as mentioned in other works [64]. However, no statistical differences between formulations were found, except for usNLCsST *vs.* usNLCs$^{c(RGDfK)}$ at 24 hours.

4.2.2. Permeability studies

The BBB was modelled using Transwell® devices in which the HBMEC were grown for 7 days until monolayer formation. The BBB characteristics were assessed by the transendothelial electrical resistance (TEER) to evaluate the tightness of the resulting barrier. TEER
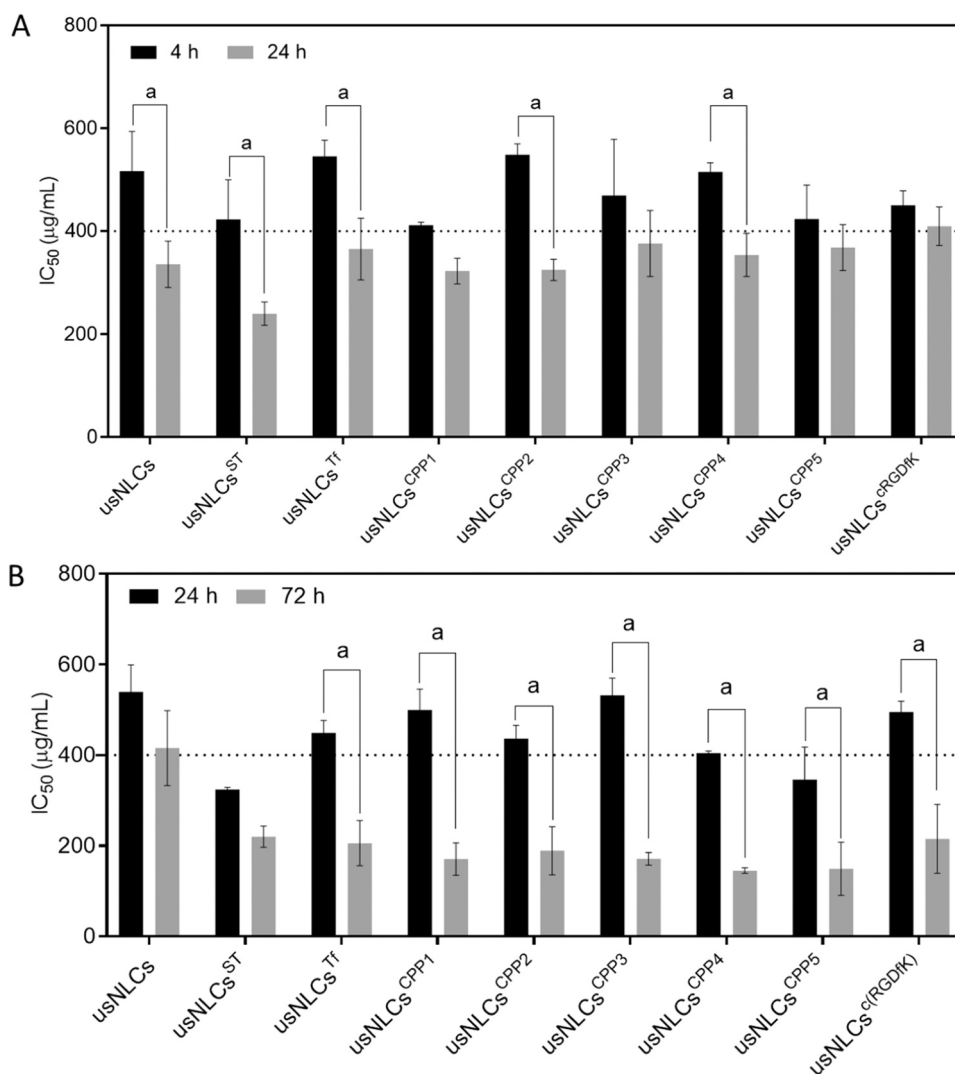
Fig. 4. A) *In vitro* cytotoxic effect, as IC_{50}, of different CXB-loaded usNLCs incubated with HBMEC cells for 4 and 24 hours. Data are expressed as mean ± SD (n = 9, [a] $p < 0.0001$). B) *In vitro* cytotoxic effect, as IC_{50}, of loaded-usNLCs incubated with U87 cells for 24 hours and 72 hours. Data are expressed as mean ± SD (n = 9, [a] $p < 0.0001$).

values were, on average 120–150 $\Omega{*}cm^2$ when initiating the experiments [65]. Considering the lipid content, CXB-loaded usNLCs were placed in the upper compartment with a 400 μg/mL concentration. IC_{50} values at 4 hours were used as a reference. Despite the usNLCs concentration is close to the IC_{50} at 4 hours, and the possibility of breaking the BBB integrity is higher, both TEER and Lucifer yellow were used to confirm the BBB integrity. The P_{app} value of Lucifer yellow below 2.8 $\times 10^{-5}$ cm/s suggests no adverse effect on cell monolayer integrity, confirmed by TEER values after 4 hours (120–150 $\Omega.cm^2$).

The quantification of CXB in the basal compartment at 0.5, 1, 2, and 4 hours, after three independent experiments, is depicted in Fig. S1 (A and B) and Table 6. These results account for both entrapped and released CXB. usNLCs were used as the negative control, and usNLCs^{Tf} as a positive control. Results show that the rank of transport ratio across the BBB was usNLCs^{Tf} > usNLCs^{CPP4}~usNLCs > usNLCs^{CPP2} > usNLCs^{CPP3} > usNLCs^{CPP5} > usNLCs$^{c(RGDfK)}$ > usNLCs^{CPP1} > usNLCsST at 4 hours, indicating that Tf (P_{app} = 10.9±1.2 $\times 10^{-5}$ cm/s) and CPP4 (P_{app} = 7.3±2.9 $\times 10^{-5}$ cm/s) promote a higher drug transport across the BBB. Transferrin interacts with the BBB by a mechanism of receptor-mediated endocytosis, enhancing the potential permeability of usNLCs through the BBB, as expected based on the Tf receptors expressed on the BBB. In turn, CPP4 showed similar behavior compared to non-functionalization nanoparticles (see Table 6) and the highest permeability effect

Table 6
Apparent permeability coefficient (P_{app}) values and the ratio of CXB-loaded usNLCs with different target molecules. Data are expressed as mean ± SD (n = 3), * $p < 0.05$ and **** $p < 0.0001$ usNLCsST *vs.* usNLCs^{Tf}, non-functionalized usNLCs *vs.* functionalized-usNLCs (ST and Tf).

Formulations	P_{app} (cm/s) x 10^{-5}	Ratio usNLCs	Ratio usNLCs^{Tf}
usNLCs	7.4±0.1	1	
usNLCsST	3.9±1.3	0.5±0.2*	0.4±1.0****
usNLCs^{Tf}	10.9±1.2	1.5±0.2*	1
usNLCs^{CPP1}	4.3±0.8	0.6±0.1	0.4±0.1
usNLCs^{CPP2}	5.6±0.8	0.8±0.1	0.5±0.1
usNLCs^{CPP3}	5.5±0.6	0.7±0.1	0.5±0.1
usNLCs^{CPP4}	7.3±2.9	1.0±0.4	0.7±0.3
usNLCs^{CPP5}	4.5±0.4	0.6±0.1	0.4±0.0
usNLCs^{cRGDfK}	4.6±1.8	0.6±0.2	0.4±0.2

compared to other CPPs. CPP2 (P_{app} = 5.6 ± 0.8 $\times 10^{-5}$ cm/s) and c (RGDfK) (P_{app} = 4.6±1.8 $\times 10^{-5}$ cm/s) promoted a higher permeability than usNLCsST (P_{app} = 2.4±0.5 $\times 10^{-5}$ cm/s). It is unclear why this behavior is observed. However, an increase in the degree of interaction with the cells is hypothesized as a possible cause for the reduction in the ratios observed for the remaining biomolecule-modified formulations.

Despite this, the amount of CXB permeated through the cellular monolayer did not significantly differ among formulations with CPPs (Fig. S1 B). Moreover, no significant difference was observed among the different CPPs functionalized usNLCs in comparison to non-functionalized usNLCs.

The blank assay using a membrane without cells showed higher drug release for all the nanoparticles. However, the drug release did not reach 100% due to the lipophilic nature of the nanoparticles. This indicates that the membrane interfered with the permeability of NPs, a retention phenomenon already described in the literature [66].

4.2.3. Cellular uptake and internalization pathway

After the administration of usNLCs, the nanoparticles come into contact with the BBB cells, which is the first barrier that usNLCs must overcome to reach the brain tumor. To study the cellular uptake of usNLCs by BBB cells, HBMEC were incubated with IR780-loaded usNLCs and analyzed by flow cytometry. IR780 was not covalently bound to usNLCs, which opens the possibility that IR780 might be released from the nanoparticles during the cellular uptake. Note, however, that given the lipophilicity of IR780 (log P = 6.62) and the fact that nanoparticles were purified before use, it could be considered a good marker for

nanoparticle tracking. To eliminate any interference, cells were incubated with free IR780, unloaded usNLCs, and IR780-loaded usNLCs separately under the same conditions. The formulations studied had different molecules attached to the surface. usNLCs was used as a negative control, and usNLCs^{Tf} was used as a positive control to compare the effect with CPPs. CPPs present advantages over Tf, such as lower molecular weight, feasibility of synthesis, flexibility in derivatization, and physicochemical parameters compatible with their role in active targeting, compared with standard proteins, including the small size (less than 30 residues) with the ability to cross biological membranes in an energy-dependent or -independent manner. The kinetics of brain uptake via adsorptive-mediated transport or receptor-mediated transport across the BBB is slow, and both are saturable transport processes. The main difference is that adsorptive-mediated transport requires higher levels of concentration than receptor-mediated transport [67].

The quantitative intracellular uptake in HBMEC of the IR780 loaded-usNLCs was analyzed by flow cytometry, and Fig. 5 shows the results at different time points (0.5, 1, 2, and 4 hours). Table S5 displays the ratios considering the IR780 encapsulation (usNLCs/IR) and surface functionalization (usNLCs^{Functionalized}/usNLCs) and clears the way for a comparative analysis between the formulations. The fluorescence
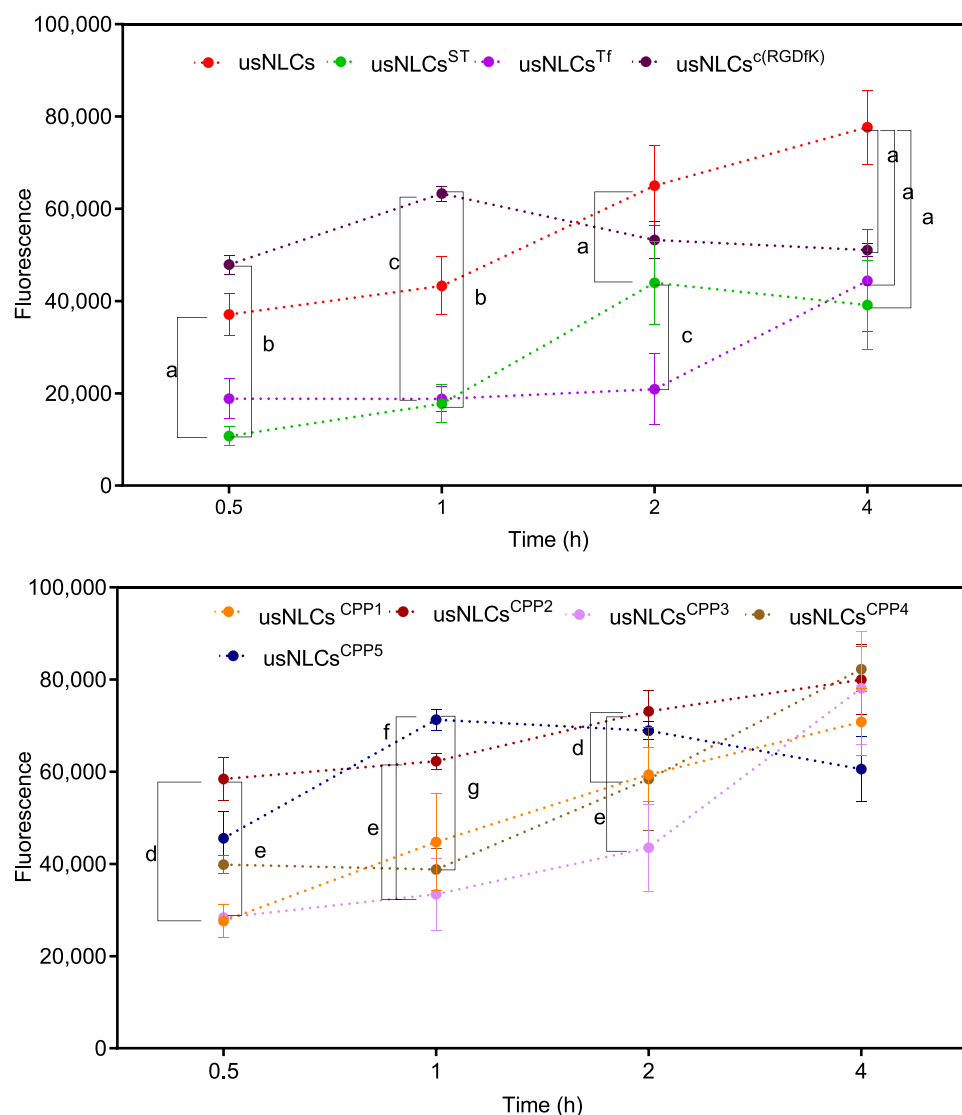

Fig. 5. *In vitro* cellular uptake of IR780 loaded-usNLCs following 0.5, 1, 2, and 4 hours of incubation with HBMEC cells. Data are expressed as mean ± SD (n = 27, which stands for 9 replicates for 3 days, [a, b, c, d, e, f, g] *p*<0.0001). Note that each time point corresponds to different wells containing independently seeded cells. Therefore, the assays were made independently per time point.

intensity in cells increased gradually along with incubation time without toxicity. The results support the encapsulation potential, regardless of the usNLCs functionalization (usNLCs/IR>1). Similar uptake was observed for the usNLCs^{Tf} and usNLCsST, indicating that the amount of usNLCs taken up by the HBMEC was the lowest (usNLCs^{Functionalized}/usNLCs was lower than 1). In contrast, usNLCs^{CPP5}>usNLCs^{c}$^{(RGDfK)}$>usNLCs^{CPP2} showed the highest cellular uptake, with remarkably higher internalization effect than other functionalized usNLCs, mainly at the first time points (0.5 and 1 hours, usNLCs$^{c(RGDfK)}$ *vs.* usNLCsST, $p < 0.0001$); the usNLCs^{CPP1}~usNLCs^{CPP4}>usNLCs^{CPP3} had a higher internalization at longer time points (0.5 hours *vs.* 4 hours, $p < 0.0001$). However, it is interesting to highlight the advantage of higher uptake in the BBB cells early (0.5 and 1 hours).

Besides assessing the extent of cellular uptake, it is important to inspect the internalization pathways of nanoparticles through the BBB. Nanoparticles can enter cells passively, in an energy-independent mechanism, or actively, in an energy-dependent mechanism, the latter

preferentially occurring at 4 °C, where the pathways dependent on energy are inhibited. There are distinct internalization pathways for nanoparticles to enter cells, and they can be divided into non-endocytic (*e.g.,* pore formation, inverted micelle formation, or carpet model) and endocytic paths (*e.g.,* caveolae-mediated endocytosis, clathrin-mediated endocytosis or macropinocytosis) [68]. Several factors influence nanoparticle-cell interaction, including size, charge, shape, functional groups, protein corona, folding ability, rigidity, and amphipathicity. All factors together make the internalization process a complex one.

To classify nanoparticle transport pathways as energy-dependent or non-energy-dependent, the cells were preincubated at 4 °C. The outcomes revealed that the fluorescent intensity did not significantly decrease (% inhibition < 50%) compared to the cells treated in normal conditions (37 °C, see Fig. 6 A). This outcome indicates that active transport mechanisms may be involved despite not being the main pathway used by the different usNLCs formulations. Note that usNLCs formulations can cross the cell membrane by a non-endocytic pathway
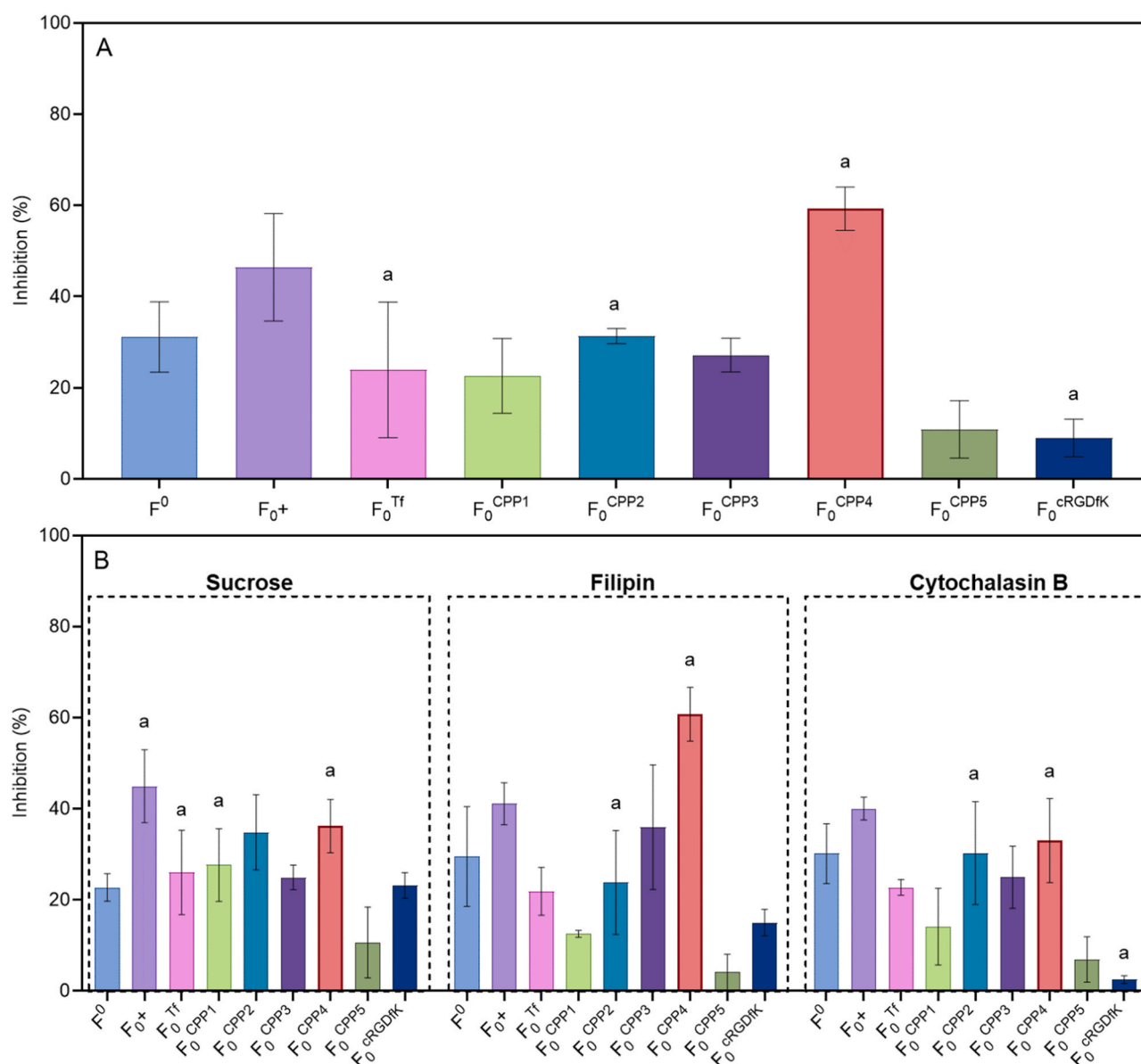

Fig. 6. Inhibition of internalization of IR780-loaded usNLCs in HBMEC cells at 4 °C (A, low temperature) and in the presence of different inhibitors (B, sucrose, fillipin, and cytochalasin B, respectively). Data are expressed as mean ± SD (n = 27, which stands for 9 replicates for 3 days, [a] $p<0.0001$ considering the normal conditions and [b] $p<0.0001$ considering the usNLCs (F$_0$) at each condition. A t-test was considered to evaluate the statistical significance of each condition. In turn, a one-way ANOVA with Dunnet's multiple comparisons was employed for evaluating the impact of surface modification per condition.

(*e.g.*, direct translocation, an energy-independent pathway). Although fluorescence did not decrease significantly in cellular uptake studies performed at low temperatures (4 °C), cells were preincubated with pharmacological inhibitors (sucrose, filipin, and cytochalasin B, see Fig. 6 B) to distinguish the endocytosis mechanism. The usNLCs uptake results were expressed as relative fluorescence, considering the fluorescence in the cells after incubation in the presence of inhibitors and the fluorescence of the cells incubated under normal conditions (2 hours at 37 °C, assumed as 100%). The uptake was not different from that at low temperatures when cells were co-incubated with cytochalasin B (inhibitor of pinocytosis), sucrose (inhibitors of clathrin-dependent endocytosis), and filipin II (inhibitor of caveolae-mediated endocytosis), except for usNLCs^{CPP4}. Again, the results suggest that usNLCs uptake was mediated by direct translocation, and some usNLCs by caveolae-mediated endocytosis, as of all the inhibitors, filipin promoted a higher inhibition (particle size range 60–80 nm), as shown in Fig. 6 B. In addition, internalization of usNLCs modified with c(RGDfK) or CPP5 was not significantly inhibited. Taken together, these results suggest that cellular internalization of usNLCs occurs largely via a non-dependent energy pathway (*e.g.*, direct translocation). CPP-usNLCs formulations exhibited a similar uptake level at a low temperature and in the presence of inhibitors. Endocytosis is not exclusive, and it was accompanied by direct translocation, which justifies the ambiguous results.

4.3. In vitro studies upon U87 cells

4.3.1. Cytotoxicity studies

The antitumor efficacy of usNLCs in U87 cells was examined by quantifying the percent tumor cell viability using the resazurin test and IC$_{50}$ calculation at 24 hours and 72 hours (Fig. 4 B). As expected, cell viability decreases from 24 hours to 72 hours in a concentration-dependent manner, and these differences are statistically significant ($p < 0.0001$). As mentioned earlier, usNLCsST exhibited higher cytotoxicity than the other usNLCs at 24 hours. However, the stearylamine effect at 72 hours was not different from that at 24 hours. After 72 hours, the impact of different peptides was not discriminatory among formulations. Notably, functionalized usNLCs showed an inhibitory effect on U87 cells for the longest time.

4.3.2. Cellular uptake and internalization pathways

The cellular uptake of different IR780 loaded-NLCs was quantitatively evaluated by measuring the fluorescence intensity. The cells were incubated with usNLCs for different time points (1, 2, 4, and 8 hours). Fig. 7 shows the fluorescence intensity. Two controls were used, including a negative control without treatment, and no fluorescence in
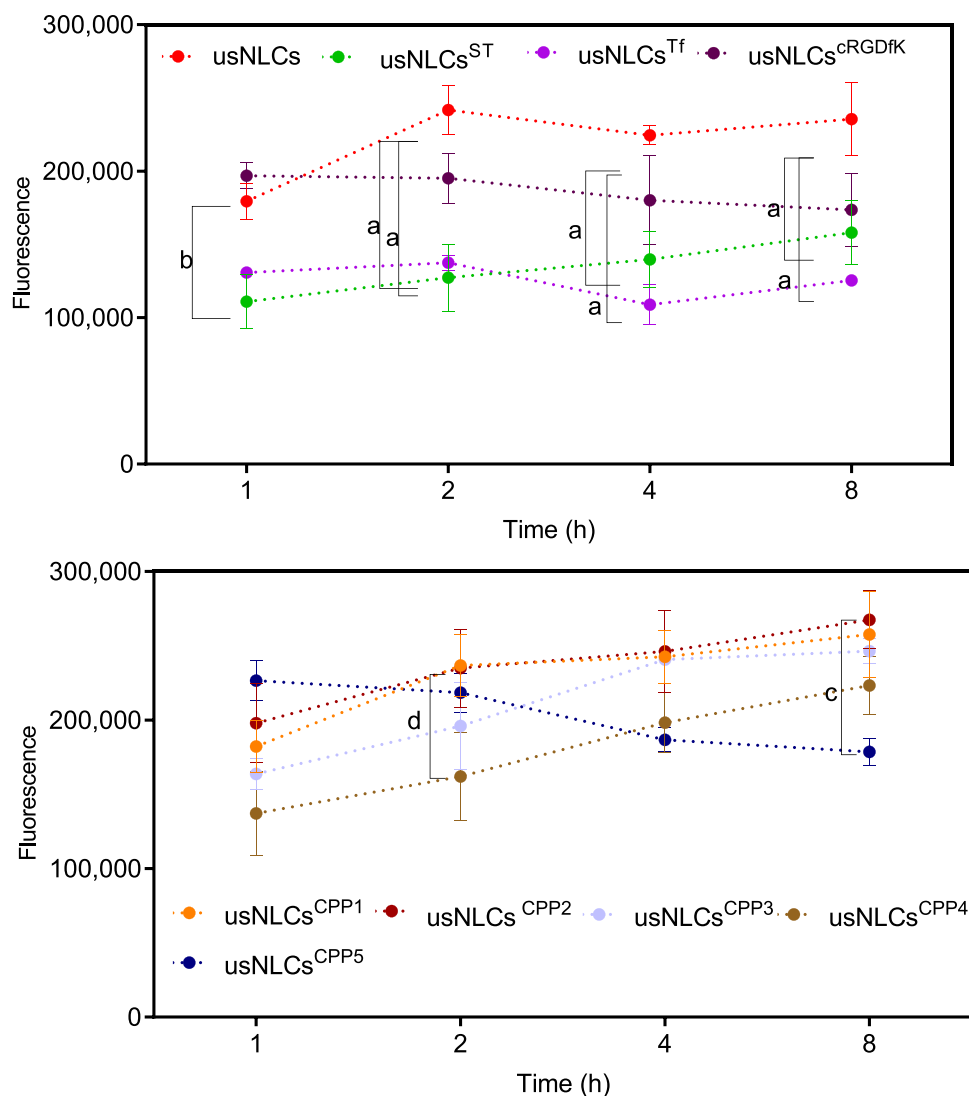

Fig. 7. The cellular uptake of fluorescent IR780 loaded usNLCs in U87 cells at 1, 2, 4, and 8 hours. Data are expressed as mean ± SD (n = 27, which stands for 9 replicates for 3 days, $^{a, b, c, d}$ $p < 0.0001$).

U87 cells was observed, and a positive control using the IR780 free to discard the possibility of the IR780 being released from nanoparticles. Cells treated with free IR780 exhibited the same fluorescence intensity over time (data not shown). usNLCs exhibited increased fluorescence intensity over 8 hours and higher uptake than free IR780. The results indicate that usNLCs are more readily and rapidly internalized in glioma than in BBB cells.

Stearylamine and transferrin promoted the lowest uptake (see Fig. 7). Stearylamine imparts a positive charge to the surface of usNLCs (ZP = + 36±5 mV), which in theory, is an advantage for the close contact between NPs and negative-cell membranes [69–71]. However, stearylamine did not improve the interaction with the cell membrane. This effect could be explained by the adsorption of proteins on the surface after usNLCsST dispersion in the cell medium, leading to the formation of the protein corona (see Table S6) [72]. The cationic charge alone appears to be insufficient to ensure efficient uptake. The usNLCs coated with transferrin showed lower cellular uptake due to lower TfRs in U87 cells.

On the other hand, usNLCs, usNLCs^{CPP1}, usNLCs^{CPP2}, usNLCs^{CPP3}, usNLCs^{CPP5}, and usNLCs$^{c(RGDfK)}$ demonstrated higher interaction with the U87 cell membrane (see Table S6). The presence of these peptides can influence the uptake efficiency of usNLCs. Those results are important because a highly significant accumulation of usNLCs in the tumor allows a more prolonged drug release and, consequently, more effective treatment. Also, this finding suggests that active targeting with CPP2 and CPP3 (see Fig. 7) allows a higher interaction of usNLCs with the cell membranes, enhancing the uptake of IR780 during the 8 hours. Conversely, differences in the uptake of HBMEC cells were not found, which may indicate that CPP2 and CPP3 address higher affinity to target glioma cells than endothelial cells. CPP4 also showed no significant interaction with U87 cells, in contrast with the best behavior exhibited in BBB cells regarding permeability and cellular uptake. Note the structural similarity with pVEC, an efficient cell-penetrating peptide exhaustively studied in the respective interaction with the BBB [73]. Overall, these results suggest that CPP2 and CPP3 significantly favor cell uptake in U87, while CPP4 is more effective for HBMEC cells.
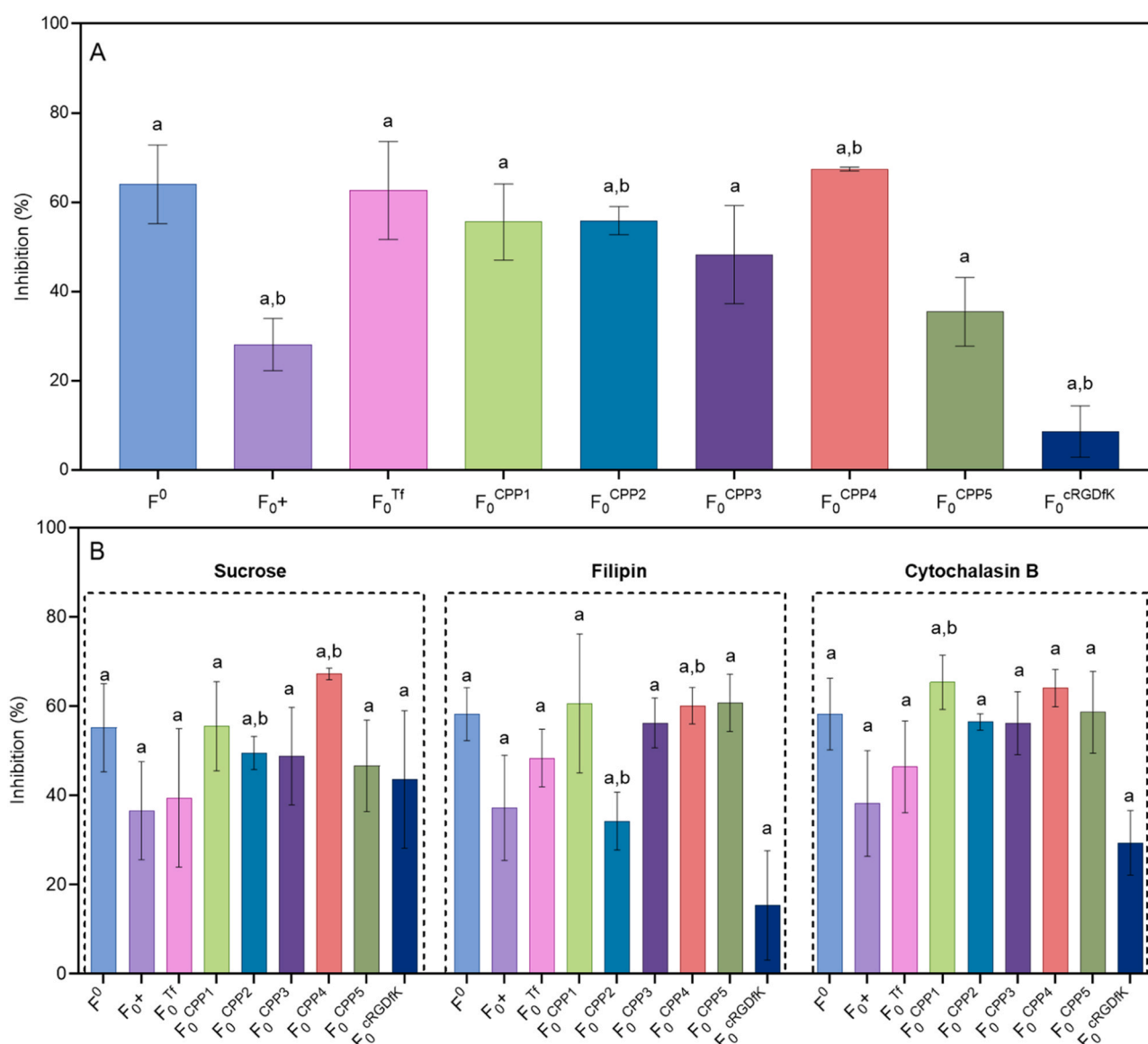

Fig. 8. Inhibition at 4 °C (A, low temperature) and different inhibitors (B, sucrose, fillipin, and cytochalasin B, respectively) on IR780-loaded usNLCs internalization in U87 cells. Data are expressed as mean ± SD (n = 27, which stands for 9 replicates for 3 days, ^{a} $p<0.0001$ considering the normal conditions and ^{b} $p<0.0001$ considering the usNLCs (F_0) at each condition). Again, a t-test was considered to evaluate the statistical significance of each condition. In turn, a one-way ANOVA with Dunnet's multiple comparisons was employed for evaluating the impact of surface modification per condition.

The mechanisms involved in this process were inspected after studying the extent of cellular internalization of usNLCs in glioblastoma cells. A statistically significant reduction (<50%) in cell uptake (see Fig. 8 A) was observed when compared with the formulation under normal conditions (37 °C), except for usNLCs functionalized with stearylamine (usNLCsST). That decrease points out endocytosis as an internalization mechanism of usNLCs uptake. The c(RGDfK), a tumor-targeting peptide, is receptor-mediated and energy-dependent, with a high affinity to $\alpha_v\beta_3$ and $\alpha_v\beta_5$ integrin receptors expressed on glioma cells [74,75]. The c(RGDfK) result was not predictable as this peptide has been described as an active targeting strategy for glioma cell lines [74,75]. Although c(RGDfK) did not exhibit an internalization mechanism by endocytosis, usNLCs$^{c(RGDfK)}$ were internalized by direct translocation. Again, the inhibition of endocytosis was not complete, which means that usNLCs can cross the cell membrane by direct translocation but on a smaller scale than the results obtained in BBB cells.

Again, three different inhibitors were used to identify the endocytosis pathway: cytochalasin B, sucrose, and filipin II (see Fig. 8 B). These uptake results suggest that usNLCs may be taken up via multiple endocytic pathways and imply that they rely mainly on caveolae-mediated endocytosis, followed by clathrin-dependent endocytosis. The observations are consistent with our previous studies in which glycerol-based and conjugated peptides (HA-c[RGDfK]) usNLCs are designed to interact with cancer cells [25,50]. The stearylamine-based formulation was less affected by temperature or pharmacological inhibitors and could cross the cell membrane by direct translocation.

The cellular uptake of usNLCs exhibited dependence on both surface modification and cell type. Despite the inhibitory effect on endocytic pathways being higher in glioma cells, the internalization pathway (caveolae, clathrin, or macropinocytosis) used by nanoparticles is not clear. This phenomenon can be explained by direct translocation and the parallel involvement of more than one pathway.

The impact of the surface modification on the cellular *in vitro* performance was evaluated using unsupervised learning algorithms, including hierarchical cluster analysis (HCA) and principal component analysis (PCA). In HCA, the distance between formulations and biorecognized molecules was calculated using the Euclidian metric and the Ward linkage. PCA was performed using the Row-wise estimation method and the correlation matrix. Both HCA and PCA were used to explore similarities, hidden molecular patterns, and differences among targeting molecules, for which the interactions within the data are not readily visible.

These methods allowed to evaluate the qualitative effects of physicochemical properties of the targeting molecules on cytotoxicity, cellular uptake, and permeability studies, considered as critical quality attributes (CQAs). The data set analyzed was composed of seven molecular descriptors, including the molecular weight (MW), logarithm of the partition coefficient (log P), pKa, the hydrophilic residues, the number of amine groups (coded as -NH$_2$ residues), the charge that molecules provide to the usNLCs surface in water (coded as ChargeNPs), and the polar surface area (PSA) for the interaction between usNLCs and HBMEC and U87 cells.

The dendrograms depicted in Fig. S2 and S3 enable the establishment of the similarity profiles for the different recognized molecules according to the mean values of the CQAs. Fig. S2 A reflects the behavior of the formulations on HBMEC. Fig. S2 B reproduces the pattern of each cluster according to the CQAs considered for the *in vitro* cellular performance evaluation. From Fig. S2 A, four clusters were identified: Cluster 1 (in red color corresponding to ST) included a higher cytotoxic effect, and Cluster 2 (in green color corresponding to Tf) was composed of the most biocompatible nanoparticles, with increased permeability through the HBMEC. However, both clusters included nanoparticles with lower values in cellular uptake. Cluster 3 (in blue color corresponding to CPP1, CPP2, CPP3, and CPP4) includes the formulations evidencing the most balanced response across CQAs, also gathered nanoparticles with a higher internalization in HBMEC at 4 hours, while Cluster 4 (in gold color referring to CPP5 and c[RGDfK]) gathered the nanoparticles with an increased internalization in the first hour, and biocompatibility to HBMEC cells.

Fig. S3 A shows the overall correlation between the formulations and the U87 cells. Fig. S3 B depicts the impact of each cluster on the *in vitro* cellular performance, following the distinct CQAs considered. Fig. S3 A displays again four natural clusters: Cluster 1 (red color, ST, and Tf) contains the formulations with the worst behavior in glioma cells, represented by the lower cellular uptake. Cluster 2 (green color, CPP1, CPP2, and CPP3), 3 (blue color, c[RGDfK]), and 4 (gold color, CPP4 and CPP5) segregated the formulations with higher internalization values and showing an increased ability to target the glioma cells. The main difference between these groups was the biocompatibility of the targeting molecules, with cluster 3 displaying the highest IC$_{50}$, *i.e.*, the highest biocompatibility, whilst cluster 4 resembled the highest cytotoxic effect.

The relative interaction and the impact of physicochemical characteristics of targeting molecules and the *in vitro* performance of formulations were also explored using PCA (Fig. 9). Variables for PCA were MW, log P, pKa, hydrophilic residues, -NH$_2$ residues, ChargeNPs, and PSA, while targeting molecule descriptors and apparent permeability (P$_{app}$) coefficient, cytotoxicity in HBMEC (CBBB4 and CBBB24) and U87 (CG24 and CG72), and cellular uptake in HBMEC (CU0.5BBB, CU1BBB, CU2BBB, and CU4BBB) and U87 (CU1G, CU2G, CU4G and CU8G), as CQAs. The biplot depicted in Fig. 9 shows the relative positioning of the functionalized-usNLCs (blue points) and the contributions of each variable (colored vectors) on the two principal components (PCs) with an information recovery of 70.7%. Formulations that are close together in the biplot display similar properties and performance. These similarities align with the groups previously identified, reflecting the overall behavior after assembling both cell lines. The magnitude of the vectors reflects the impact of the variables on each principal component. The higher the magnitude of the vector, the greater the impact of the variable on the principal component. The direction of the vector is also an indicator of the growth and evolution of the variable's value. Relevant correlations between variables can also be inferred by inspecting the angles between vectors. The smaller the angle between two variables, the higher is the correlation.

In essence, three clusters can be identified: one corresponding to transferrin (Tf), a second one to stearylamine (ST), and a third one to peptides (CPPs and TPP). In what concerns the Tf, it is evident that this biorecognized molecule is the main responsible for the increase in apparent permeability through the BBB, with molecular weight (MW) and the number of NH$_2$ residues as the most influencing descriptors. This counterproduced effect seems to reflect the internalization mechanism involved, in other words, taking advantage of the ligand-receptor-mediated internalization.

Regarding the ST, the NP positive charge assigned by this molecule, followed by the log P, are the principal contributors to the incremental cytotoxicity, not significantly impacting the cellular uptake behavior.

In relation to the third cluster, this comprises the influence of the peptides essentially materialized on the NP cellular uptake extent. In this case, pKa arises as the major descriptor of their pattern. This can be explained by the divergency in the internalization pathways involved since, conversely to Tf, CPP exerts its impact on the basis of non-energy-dependent mechanisms stemming from electrostatic interactions with the cellular membrane, as previously described.

Within peptides, CPP2 is pointed out as the best performant considering both HBMEC and U87 cell lines (see, *e.g.*, CU1G and CU1BBB loadings). In turn, CPP4 exhibits a more favorable trend to cross BBB along with a lower cytotoxic effect. This is considered neutral in what concerns c(RGDfK) since a non-significant impact is denoted.

Also, it can be rationalized that MW, -NH$_2$ residues, and pKa are the variables with the greatest contribution to PC1. In the case of HBMEC, the apparent permeability coefficient (P$_{app}$) and cellular uptake (at 1 and 2 hours) also have an important impact on PC1, suggesting that
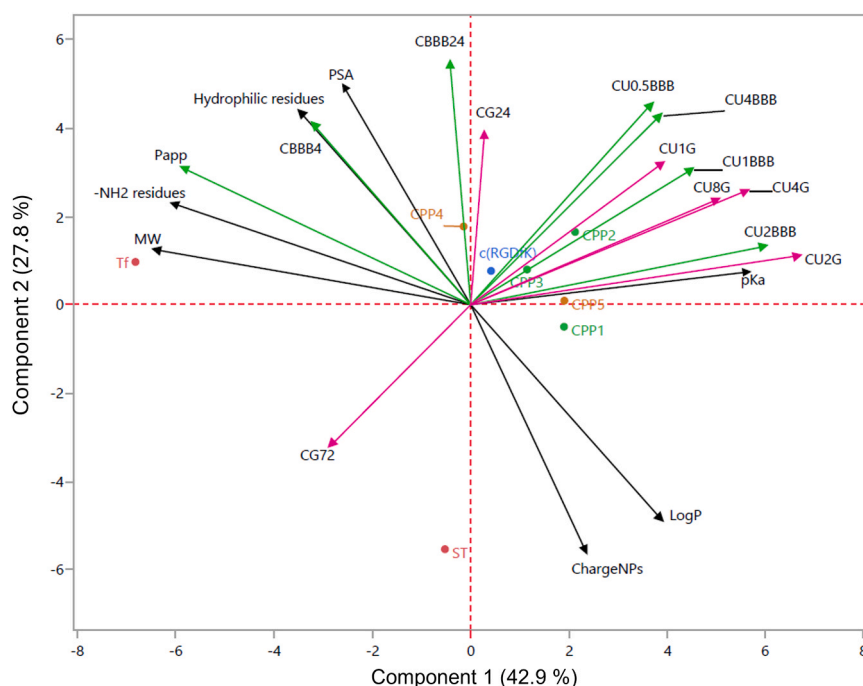
Fig. 9. Biplot representation of the eight functionalized-usNLCs, the corresponding *in vitro* performance, and physicochemical characteristics of targeting molecules on the first two PCs (42.9% and 27.8% of initial information recovery, respectively). The black arrows represent the physicochemical properties of targeting molecules; the green arrows represent the *in vitro* performance in HBMEC cells; the purple arrows represent the *in vitro* performance in U87 cells; and the blue points are the formulations. Key: CBBB4 – Cytotoxicity in HBMEC at 4 hours; CBBB24 – Cytotoxicity in HBMEC at 24 hours; Papp – permeability apparent coefficient; CU1BBB – cellular uptake at 0.5 hours in HBMEC; CU1BBB – cellular uptake at 1 hour in HBMEC; CU2BBB – cellular uptake at 2 hours in HBMEC; CU4BBB – cellular uptake at 4 hours in HBMEC; CG24 – Cytotoxicity in U87 cells at 24 hours; CG72 – Cytotoxicity in U87 cells at 72 hours; CU1G – cellular uptake at 1 hour in U87 cells; CU2G – cellular uptake at 2 hours in U87 cells; CU4G – cellular uptake at 4 hours in U87 cells; CU8G – cellular uptake at 8 hours in U87 cells.

molecules with high MW, -NH$_2$ residues, and low pKa tend to facilitate the transport through the BBB. On the other hand, smaller molecules with high pKa can display higher internalization but lower permeability through the 2D-BBB model. In the U87 cells, the highlighted features that benefit cellular uptake follow the same trend described above. These results suggest that CPP4 and Tf were also effective in increasing the permeability through the BBB, in contrast to ST. PC2 is more directly related to log P, ChargeNPs, PSA, and hydrophobic residues. The increase in positive charge on the surface of NPs led to an increase in cytotoxicity in both cell lines. This highlights that the selection of the biorecognized molecule for NP surface functionalized should not be randomly conducted, since variations in *in vitro* cellular performance can be noteworthy observed.

4.4. Drilling down the data

In what follows, the more relevant observations are summarized:

- usNLCs can be functionalized with different biorecognized molecules by electrostatic interaction: cationic surfactants, cell-penetrating peptides, tumor-targeting peptides, and proteins.
- The functionalization is effective to revert the zeta potential of bare usNLCs.
- The adsorption CPP-NPs patterns are consistent with ZP behavior.
- The positive charge alone appears to be insufficient to ensure efficient uptake, and it is lost through the formation of the protein corona.
- Targeting molecules, such as CPPs or TTP, protect the usNLCs from the protein corona formation.
- Transferrin showed to be efficient in permeability studies.
- CPPs exhibited a controversial behavior in terms of internalization pathways, depending on the surface modification (composition of CPPs) or cell types (HBMEC *vs.* U87).

- CPPs were internalized to a large extent by non-energy dependent pathways due to the electrostatic interaction.
- usNLCs uptake was mediated by direct translocation, and by caveolae-mediated endocytosis (particle size range 60–80 nm).
- CPP4 demonstrated the best performance in HBMEC, both in uptake and permeability studies.
- In general, CPPs-based formulations revealed higher affinity to U87 cells than to HBMEC.
- CPP2 and CPP3 improve cellular interaction in U87 cells.
- Optimal usNLCs combine dual targeting to enhance nanoparticle interaction with different cells (HBMEC – Tf or CPP4 - followed by U87 cells – CPP2 or CPP3).

5. Conclusions

Chemotherapy for glioblastoma has provided limited benefit due to the failure of drugs to penetrate the BBB and non-selective drug accumulation in the entire brain. To overcome these limitations, several active targeting molecules were evaluated for the usNLCs surface modification, including cell-penetrating peptides, tumor-targeting peptides, receptor proteins, and cationic surfactants, in order to improve the transport of the drug across the BBB and consequently target brain tumor cells. Thus, different usNLCs were characterized in what concerns (i) stability in biological conditions, (ii) cytotoxicity, (iii) permeability, and (iv) uptake to HBMEC and U87 cells. The best performance in terms of permeability in the 2D-BBB model was obtained with transferrin, followed by CPP4. However, the cellular internalization was higher for CPP4. BBB cells were more sensitive to the nanoparticles than glioblastoma cells. Functionalized-usNLCs were capable of the transportation of the CXB into living cells, and the cellular uptake mechanism was activated on more than one route in an energy-dependent or -independent manner. The internalization was 2.5 times higher in glioblastoma cells than in the BBB cells, which could be favorable in the case

of brain tumors. The identification of the endocytosis pathway for the usNLCs was not clear, being effectively internalized by direct translocation and endocytic pathways.

In conclusion, the functionalized-usNLCs developed in this work showed high affinity to BBB cells (Tf or CPP4) and tumor cells (CPP3) or for both (CPP2). The dual-targeting approach of usNLCs could significantly contribute to BBB transport and tumor growth inhibition. Overall, this work reinforces the need to carry out this "whole-picture approach" when inspecting their impact on interface properties in the pharmaceutical development of surface-functionalized nanosystems.

Funding

CRediT authorship contribution statement

Maria Mendes: Writing – original draft, Investigation, Formal analysis, Data curation, Conceptualization. **Sandra Nunes:** Formal analysis, Data curation. **Tânia Cova:** Formal analysis, Data curation. **Francisco Branco:** Methodology. **Michael Dyrks:** Resources. **Beate Koksch:** Resources. **Nuno Vale:** Resources. **João J Sousa:** Supervision, Resources. **Alberto Pais:** Writing – review & editing, Supervision. **Carla Vitorino:** Writing – review & editing, Supervision, Formal analysis, Data curation, Conceptualization.

Declaration of conflict of interests

The authors declare no conflicts of interest.

Data availability

Data will be made available on request.

Acknowledgements

Appendix A. Supporting information

Supplementary data associated with this article can be found in the online version at doi:10.1016/j.colsurfb.2024.113983.

References

[1] H. Sung, J. Ferlay, R.L. Siegel, et al., Global cancer statistics 2020: GLOBOCAN estimates of incidence and mortality worldwide for 36 cancers in 185 countries, CA Cancer J. Clin. 71 (3) (2021) 209–249, https://doi.org/10.3322/caac.21660.

[2] A. Bhowmik, R. Khan, M.K. Ghosh, Blood-brain barrier: a challenge for effectual therapy of brain tumors, Biomed. Res Int 2015 (2015), https://doi.org/10.1155/2015/320941.

[3] H. Kadry, B. Noorani, L. Cucullo, A blood–brain barrier overview on structure, function, impairment, and biomarkers of integrity, Fluids Barriers CNS 17 (1) (2020) 1–24, https://doi.org/10.1186/s12987-020-00230-3.

[4] W.J. Geldenhuys, A.S. Mohammad, C.E. Adkins, P.R. Lockman, Molecular determinants of blood–brain barrier permeation, Ther. Deliv. 6 (8) (2015) 961–971, https://doi.org/10.4155/tde.15.32.

[5] W.M. Pardridge, Drug transport across the blood–brain barrier, J. Cereb. Blood Flow. Metab. 32 (11) (2012) 1959–1972, https://doi.org/10.1038/jcbfm.2012.126.

[6] H.L. Wong, X.Y. Wu, R. Bendayan, Nanotechnological advances for the delivery of CNS therapeutics, Adv. Drug Deliv. Rev. 64 (7) (2012) 686–700, https://doi.org/10.1016/j.addr.2011.10.007.

[7] R. Karim, C. Palazzo, B. Evrard, G. Piel, Nanocarriers for the treatment of glioblastoma multiforme: current state-of-the-art, J. Control Release 227 (2016) 23–37, https://doi.org/10.1016/j.jconrel.2016.02.026.

[8] A. Domínguez, B. Suárez-Merino, F. Goñi-de-Cerio, Nanoparticles and blood-brain barrier: the key to central nervous system diseases, J. Nanosci. Nanotechnol. 14 (1) (2014) 766–779, https://doi.org/10.1166/jnn.2014.9119.

[9] R. Dal Magro, F. Ornaghi, I. Cambianica, et al., ApoE-modified solid lipid nanoparticles: a feasible strategy to cross the blood-brain barrier, J. Control Release 249 (2017) 103–110, https://doi.org/10.1016/j.jconrel.2017.01.039.

[10] J. Emami, M. Rezazadeh, H. Sadeghi, K. Khadivar, Development and optimization of transferrin-conjugated nanostructured lipid carriers for brain delivery of paclitaxel using Box–Behnken design, Pharm. Dev. Technol. 22 (3) (2017) 370–382, https://doi.org/10.1080/10837450.2016.1189933.

[11] Y.H. Chen, L.Z. Pan, M. Jiang, D. Li, L.J. Jin, Nanostructured lipid carriers enhance the bioavailability and brain cancer inhibitory efficacy of curcumin both in vitro and in vivo, Drug Deliv. 23 (4) (2016) 1383–1392, https://doi.org/10.3109/10717544.2015.1049719.

[12] C.M. Keck, N. Baisaeng, P. Durand, M. Prost, M.C. Meinke, R.H. Müller, Oil-enriched, ultra-small nanostructured lipid carriers (usNLC): a novel delivery system based on flip–flop structure, Int J. Pharm. 477 (1-2) (2014) 227–235, https://doi.org/10.1016/j.ijpharm.2014.10.029.

[13] M. Mendes, J. Basso, J. Silva, et al., Biomimetic ultra-small lipid nanoconstructs for glioblastoma treatment: a computationally guided experimental approach, Int J. Pharm. 587 (July) (2020) 119661, https://doi.org/10.1016/j.ijpharm.2020.119661.

[14] A.R. Neves, J.F. Queiroz, B. Weksler, I.A. Romero, P.O. Couraud, S. Reis, Solid lipid nanoparticles as a vehicle for brain-targeted drug delivery: two new strategies of functionalization with apolipoprotein E, Nanotechnology 26 (49) (2015) 495103, https://doi.org/10.1088/0957-4484/26/49/495103.

[15] H. Gao, Z. Yang, S. Zhang, et al., Ligand modified nanoparticles increases cell uptake, alters endocytosis and elevates glioma distribution and internalization, Sci. Rep. 3 (2013) 2534, https://doi.org/10.1038/srep02534.

[16] D. Raucher, Tumor targeting peptides: novel therapeutic strategies in glioblastoma, Curr. Opin. Pharm. 47 (2019) 14–19, https://doi.org/10.1016/j.coph.2019.01.006.

[17] E.L. Al Humaidan, S.L. Pedersen, A. Burkhart, et al., The cell-penetrating peptide tat facilitates effective internalization of PSD-95 inhibitors into blood–brain barrier endothelial cells but less efficient permeation across the blood–brain barrier in vitro and in vivo, Front Drug Deliv. 2 (2022) 854703, https://doi.org/10.3389/fddev.2022.854703.

[18] M.C. Wu, E.Y. Wang, T.W. Lai, TAT peptide at treatment-level concentrations crossed brain endothelial cell monolayer independent of receptor-mediated endocytosis or peptide-inflicted barrier disruption, PLoS One 18 (10) (2023) e0292681, https://doi.org/10.1371/journal.pone.0292681.

[19] X. Li, X. Pu, X. Wang, et al., A dual-targeting peptide for glioblastoma screened by phage display peptide library biopanning combined with affinity-adaptability analysis, Int J. Pharm. 644 (2023) 123306, https://doi.org/10.1016/j.ijpharm.2023.123306.

[20] L. Lu, L. Wang, L. Zhao, et al., A novel blood–brain barrier-penetrating and vascular-targeting chimeric peptide inhibits glioma angiogenesis, Int J. Mol. Sci. 24 (10) (2023) 8753, https://doi.org/10.3390/ijms24108753.

[21] D. Zhang, J. Kong, X. Huang, et al., Targeted glioblastoma therapy by integrating brain-targeting peptides and corn-derived cancer cell-penetrating proteins into nanoparticles to cross blood-brain tumor barriers, Mater. Today Nano 23 (2023) 100347, https://doi.org/10.1016/j.mtnano.2023.100347.

[22] A. Mousavizadeh, A. Jabbari, M. Akrami, H. Bardania, Cell targeting peptides as smart ligands for targeting of therapeutic or diagnostic agents: a systematic review, Colloids Surf. B Biointerfaces 158 (2017) 507–517, https://doi.org/10.1016/j.colsurfb.2017.07.012.

[23] M. Mendes, J. Sousa, A. Pais, C. Vitorino, Targeted theranostic nanoparticles for brain tumor treatment, Pharmaceutics 10 (4) (2018) 181, https://doi.org/10.3390/pharmaceutics10040181.

[24] S. Ohta, E. Kikuchi, A. Ishijima, T. Azuma, I. Sakuma, T. Ito, Investigating the optimum size of nanoparticles for their delivery into the brain assisted by focused ultrasound-induced blood–brain barrier opening, Sci. Rep. 10 (1) (2020) 1–13, https://doi.org/10.1038/s41598-020-75253-9.

[25] J. Basso, M. Mendes, J. Silva, et al., Peptide-lipid nanoconstructs act site-specifically towards glioblastoma growth impairment, Eur. J. Pharm. Biopharm. 155 (August) (2020) 177–189, https://doi.org/10.1016/j.ejpb.2020.08.015.

[26] J.V. Gregory, P. Kadiyala, R. Doherty, et al., Systemic brain tumor delivery of synthetic protein nanoparticles for glioblastoma therapy, Nat. Commun. 11 (1) (2020) 5687, https://doi.org/10.1038/s41467-020-19225-7.

[27] T. Wu, T. Liu, Y. Cao, Z. Liu, Engineering macrophage exosome disguised biodegradable nanoplatform for enhanced sonodynamic therapy of glioblastoma, Adv. Mater. 34 (15) (2022) 2110364, https://doi.org/10.1002/adma.202110364.

[28] F. Ma, L. Yang, Z. Sun, et al., Neurotransmitter-derived lipidoids (NT-lipidoids) for enhanced brain delivery through intravenous injection, Sci. Adv. 6 (30) (2020) eabb4429, https://doi.org/10.1126/sciadv.abb4429.

[29] Z. Cao, X. Liu, W. Zhang, et al., Biomimetic macrophage membrane-camouflaged nanoparticles induce ferroptosis by promoting mitochondrial damage in

glioblastoma, ACS Nano 17 (23) (2023) 23746–23760, https://doi.org/10.1021/acsnano.3c07555.

[30] T. Koneru, E. McCord, S. Pawar, K. Tatiparti, S. Sau, A.K. Iyer, Transferrin: biology and use in receptor-targeted nanotherapy of gliomas, ACS Omega 6 (13) (2021) 8727–8733, https://doi.org/10.1021/acsomega.0c05848.

[31] B. Voth, D.T. Nagasawa, P.E. Pelargos, et al., Transferrin receptors and glioblastoma multiforme: current findings and potential for treatment, J. Clin. Neurosci. 22 (7) (2015) 1071–1076, https://doi.org/10.1016/j.jocn.2015.02.002.

[32] P. Sun, Y. Xiao, Q. Di, et al., Transferrin receptor-targeted PEG-PLA polymeric micelles for chemotherapy against glioblastoma multiforme, Int J. Nanomed. 15 (2020) 6673, https://doi.org/10.2147/IJN.S257459.

[33] T. Sun, H. Wu, Y. Li, et al., Targeting transferrin receptor delivery of temozolomide for a potential glioma stem cell-mediated therapy, Oncotarget 8 (43) (2017) 74451, https://doi.org/10.18632/oncotarget.20165.

[34] M. Mendes, J. Basso, J. Sousa, A. Pais, C. Vitorino Designing Ultra-Small Nanostructured Lipid Carriers: Critical Process Parameters. Published online 2020: 1-7. doi:10.3390/IECP2020-08691.

[35] D.J. Tildesley, M.P. Allen. Computer Simulation of Liquids, Clarendon Oxford, 1987, ISBN 0-19-855375-7.

[36] P. Linse, MOLSIM, version 4.0.8, Lund University, Sweden, 2004. *Google Sch There is no Corresp Rec this Ref*.

[37] P. Banerjee, T. Geng, A. Mahanty, T. Li, L. Zong, B. Wang, Integrating the drug, disulfiram into the vitamin E-TPGS-modified PEGylated nanostructured lipid carriers to synergize its repurposing for anti-cancer therapy of solid tumors, Int J. Pharm. 557 (2019) 374–389, https://doi.org/10.1016/j.ijpharm.2018.12.051.

[38] S. Parveen, S.K. Sahoo, Long circulating chitosan/PEG blended PLGA nanoparticle for tumor drug delivery, Eur. J. Pharm. 670 (2-3) (2011) 372–383, https://doi.org/10.1016/j.ejphar.2011.09.023.

[39] Y. Sano, Y. Kashiwamura, M. Abe, et al., Stable human brain microvascular endothelial cell line retaining its barrier-specific nature independent of the passage number, Clin. Exp. Neuroimmunol. 4 (1) (2013) 92–103, https://doi.org/10.1111/cen3.12001.

[40] B.P. Daniels, L. Cruz-Orengo, T.J. Pasieka, et al., Immortalized human cerebral microvascular endothelial cells maintain the properties of primary cells in an in vitro model of immune migration across the blood-brain barrier, J. Neurosci. Methods 212 (1) (2013) 173–179, https://doi.org/10.1016/j.jneumeth.2012.10.001.

[41] S. Lakkadwala, J. Singh, Co-delivery of doxorubicin and erlotinib through liposomal nanoparticles for glioblastoma tumor regression using an in vitro brain tumor model, Colloids Surf. B Biointerfaces 173 (2019) 27–35, https://doi.org/10.1016/j.colsurfb.2018.09.047.

[42] B. Poller, H. Gutmann, S. Krähenbühl, et al., The human brain endothelial cell line hCMEC/D3 as a human blood-brain barrier model for drug transport studies, J. Neurochem 107 (5) (2008) 1358–1368, https://doi.org/10.1111/j.1471-4159.2008.05730.x.

[43] R. Cecchelli, B. Dehouck, L. Descamps, et al., In vitro model for evaluating drug transport across the blood–brain barrier, Adv. Drug Deliv. Rev. 36 (2-3) (1999) 165–178, https://doi.org/10.1016/s0169-409x(98)00083-0.

[44] A.I. Ivanov, Pharmacological inhibition of endocytic pathways: is it specific enough to be useful (Published online), Exocytosis endocytosis (2008) 15–33, https://doi.org/10.1007/978-1-59745-178-9_2.

[45] D. Dutta, J.G. Donaldson, Search for inhibitors of endocytosis: intended specificity and unintended consequences, Cell Logist. 2 (4) (2012) 203–208, https://doi.org/10.4161/cl.23967.

[46] H. Hillaireau, P. Couvreur, Nanocarriers' entry into the cell: relevance to drug delivery, Cell Mol. life Sci. 66 (17) (2009) 2873–2896, https://doi.org/10.1007/s00018-009-0053-z.

[47] J.J. Rennick, A.P.R. Johnston, R.G. Parton, Key principles and methods for studying the endocytosis of biological and nanoparticle therapeutics, Nat. Nanotechnol. 16 (3) (2021) 266–276, https://doi.org/10.1038/s41565-021-00858-8.

[48] J. Basso, M. Mendes, T.F.G.G. Cova, J.J. Sousa, A.A.C.C. Pais, C. Vitorino, Analytical Quality by Design (AQbD) as a multiaddressable platform for co-encapsulating drug assays, Anal. Methods 10 (47) (2018) 5659–5671, https://doi.org/10.1039/C8AY01695J.

[49] J. Silva M. Mendes T. Cova J. Sousa A. Pais C. Vitorino Unstructured Formulation Data Analysis for the Optimization of Lipid Nanoparticle Drug Delivery Vehicles Published online 2018 8 11 10.1208/s12249-018-1078-0.

[50] J. Basso, M. Mendes, J. Silva, et al., Sorting hidden patterns in nanoparticle performance for glioblastoma using machine learning algorithms, Int J. Pharm. 592 (July) (2021), https://doi.org/10.1016/j.ijpharm.2020.120095.

[51] M. Mendes, A. Miranda, T. Cova, et al., Modeling of ultra-small lipid nanoparticle surface charge for targeting glioblastoma, Eur. J. Pharm. Sci. 117 (February) (2018) 255–269, https://doi.org/10.1016/j.ejps.2018.02.024.

[52] R. Rampado, S. Crotti, P. Caliceti, S. Pucciarelli, M. Agostini, Recent advances in understanding the protein corona of nanoparticles and in the formulation of "stealthy" nanomaterials, Front Bioeng. Biotechnol. 8 (2020) 166, https://doi.org/10.3389/fbioe.2020.00166.

[53] M. Farshbaf, H. Valizadeh, Y. Panahi, et al., The impact of protein corona on the biological behavior of targeting nanomedicines, Int J. Pharm. 614 (2022) 121458, https://doi.org/10.1016/j.ijpharm.2022.121458.

[54] S. Streck, S.S.R. Bohr, D. Birch, et al., Interactions of cell-penetrating peptide-modified nanoparticles with cells evaluated using single particle tracking, ACS Appl. Bio Mater. 4 (4) (2021) 3155–3165, https://doi.org/10.1021/acsabm.0c01563.

[55] Z. Wang, T.Y. Lee, P.C. Ho, A novel dextran-oleate-cRGDfK conjugate for self-assembly of nanodrug, Nanomed. Nanotechnol., Biol. Med 8 (2) (2012) 194–203, https://doi.org/10.1016/j.nano.2011.06.006.

[56] J. Zhang, X. Xiao, J. Zhu, et al., Lactoferrin-and RGD-comodified, temozolomide and vincristine-coloaded nanostructured lipid carriers for gliomatosis cerebri combination therapy, Int J. Nanomed. 13 (2018) 3039, https://doi.org/10.2147/IJN.S161163.

[57] Z. Shao, J. Shao, B. Tan, et al., Targeted lung cancer therapy: preparation and optimization of transferrin-decorated nanostructured lipid carriers as novel nanomedicine for co-delivery of anticancer drugs and DNA, Int J. Nanomed. 10 (2015) 1223, https://doi.org/10.2147/IJN.S77837.

[58] A. Khajavinia, J. Varshosaz, A.J. Dehkordi, Targeting etoposide to acute myelogenous leukaemia cells using nanostructured lipid carriers coated with transferrin, Nanotechnology 23 (40) (2012) 405101, https://doi.org/10.1088/0957-4484/23/40/405101.

[59] C.J. Cheng, W.M. Saltzman, Enhanced siRNA delivery into cells by exploiting the synergy between targeting ligands and cell-penetrating peptides, Biomaterials 32 (26) (2011) 6194–6203, https://doi.org/10.1016/j.biomaterials.2011.04.053.

[60] C. Vauthier, C. Schmidt, P. Couvreur, Measurement of the density of polymeric nanoparticulate drug carriers by isopycnic centrifugation, J. Nanopart. Res 1 (3) (1999) 411–418, https://doi.org/10.1023/A:1010031605547.

[61] V.P. Zhdanov, Formation of a protein corona around nanoparticles, Curr. Opin. Colloid Interface Sci. 41 (2019) 95–103, https://doi.org/10.1016/j.cocis.2018.12.002.

[62] K. Xiao, Y. Li, J. Luo, et al., The effect of surface charge on in vivo biodistribution of PEG-oligocholic acid based micellar nanoparticles, Biomaterials 32 (13) (2011) 3435–3446, https://doi.org/10.1016/j.biomaterials.2011.01.021.

[63] T.L. Moore, L. Rodriguez-Lorenzo, V. Hirsch, et al., Nanoparticle colloidal stability in cell culture media and impact on cellular interactions, Chem. Soc. Rev. 44 (17) (2015) 6287–6305, https://doi.org/10.1039/C4CS00487F.

[64] M. Mendes, A. Miranda, T. Cova, et al., Modeling of ultra-small lipid nanoparticle surface charge for targeting glioblastoma, Eur. J. Pharm. Sci. 117 (2018) 255–269, https://doi.org/10.1016/j.ejps.2018.02.024.

[65] B. Srinivasan, A.R. Kolli, M.B. Esch, H.E. Abaci, M.L. Shuler, J.J. Hickman, TEER measurement techniques for in vitro barrier model systems, J. Lab Autom. 20 (2) (2015) 107–126, https://doi.org/10.1177/2211068214561025.

[66] J.M. Rabanel, P.A. Piec, S. Landri, S.A. Patten, C. Ramassamy, Transport of PEGylated-PLA nanoparticles across a blood brain barrier model, entry into neuronal cells and in vivo brain bioavailability, J. Control Release 328 (2020) 679–695, https://doi.org/10.1016/j.jconrel.2020.09.042.

[67] F. Hervé, Nicolae Ghinea, J.M. Scherrmann, CNS delivery via adsorptive transcytosis, AAPS J. 10 (3) (2008) 455–472, https://doi.org/10.1208/s12248-008-9055-2.

[68] D.M. Copolovici, K. Langel, E. Eriste, U. Langel, Cell-penetrating peptides: design, synthesis, and applications, ACS Nano 8 (3) (2014) 1972–1994, https://doi.org/10.1021/nn4057269.

[69] E. Fröhlich, The role of surface charge in cellular uptake and cytotoxicity of medical nanoparticles, Int J. Nanomed. 7 (2012) 5577, https://doi.org/10.2147/IJN.S36111.

[70] C. Moraru, M. Mincea, G. Menghiu, V. Ostafe, Understanding the factors influencing chitosan-based nanoparticles-protein corona interaction and drug delivery applications, Molecules 25 (20) (2020) 1–37, https://doi.org/10.3390/molecules25204758.

[71] J. Li, H. Mao, N. Kawazoe, G. Chen, Insight into the interactions between nanoparticles and cells, Biomater. Sci. 5 (2) (2017) 173–189, https://doi.org/10.1039/C6BM00714G.

[72] L. Digiacomo, F. Cardarelli, D. Pozzi, et al., An apolipoprotein-enriched biomolecular corona switches the cellular uptake mechanism and trafficking pathway of lipid nanoparticles, Nanoscale 9 (44) (2017) 17254–17262, https://doi.org/10.1039/C7NR06437C.

[73] S. Stalmans, N. Bracke, E. Wynendaele, et al., Cell-penetrating peptides selectively cross the blood-brain barrier in vivo, PLoS One 10 (10) (2015) e0139652, https://doi.org/10.1371/journal.pone.0139652.

[74] S. Song, S. Mao, G. Du, X. Zhu, Novel RGD containing, temozolomide-loading nanostructured lipid carriers for glioblastoma multiforme chemotherapy, Drug Deliv. 23 (4) (2016) 1404–1408, https://doi.org/10.3109/10717544.2015.1064186.

[75] H. Hyun, Y. Yoo, S.Y. Kim, H.S. Ko, H.J. Chun, D.H. Yang, Optimization of cRGDfK ligand concentration on polymeric nanoparticles to maximize cancer targeting, J. Ind. Eng. Chem. 81 (2020) 178–184, https://doi.org/10.1016/j.jiec.2019.09.006.